

Assimilation of all-sky seviri infrared brightness temperatures in a regional-scale ensemble data assimilation system

Article

Accepted Version

Otkin, J. A. and Potthast, R. ORCID: <https://orcid.org/0000-0001-6794-2500> (2019) Assimilation of all-sky seviri infrared brightness temperatures in a regional-scale ensemble data assimilation system. *Monthly Weather Review*, 147 (12). pp. 4481-4509. ISSN 1520-0493 doi: <https://doi.org/10.1175/mwr-d-19-0133.1> Available at <https://centaur.reading.ac.uk/86258/>

It is advisable to refer to the publisher's version if you intend to cite from the work. See [Guidance on citing](#).

To link to this article DOI: <http://dx.doi.org/10.1175/mwr-d-19-0133.1>

Publisher: American Meteorological Society

All outputs in CentAUR are protected by Intellectual Property Rights law, including copyright law. Copyright and IPR is retained by the creators or other copyright holders. Terms and conditions for use of this material are defined in the [End User Agreement](#).

www.reading.ac.uk/centaur

Central Archive at the University of Reading

Reading's research outputs online

ABSTRACT

16 Ensemble data assimilation experiments were performed to explore the abil-
17 ity of all-sky infrared brightness temperatures and nonlinear bias corrections
18 (BC) to improve the accuracy of short-range forecasts used as the prior anal-
19 yses during each assimilation cycle. Satellite observations sensitive to clouds
20 and water vapor in the upper troposphere were assimilated at hourly intervals
21 during a 3-day period. Linear and nonlinear conditional biases were removed
22 from the infrared observations using a Taylor series polynomial expansion of
23 the observation-minus-background departures and BC predictors sensitive to
24 clouds and water vapor or to variations in the satellite zenith angle. Assimi-
25 lating the all-sky brightness temperatures without BC degraded the analyses
26 based on comparisons to radiosonde observations. Bias-correcting the satel-
27 lite observations substantially improved the results, with predictors sensitive
28 to the location of the cloud top having the largest impact. Experiments em-
29 ploying the observed cloud top height or observed brightness temperatures as
30 the bias predictor generally had the smallest errors because the cloud-sensitive
31 BC predictors were able to more effectively remove large conditional biases
32 for lower brightness temperatures associated with a deficiency in upper-level
33 clouds in the model analyses. Additional experiments showed that it is benefi-
34 cial to use higher order nonlinear BC terms to remove the bias from the all-sky
35 satellite observations. This was demonstrated by the tendency for the higher
36 order predictors to have a neutral-to-positive impact on the temperature and
37 wind fields, while also greatly improving the cloud and water vapor fields.

38 **1. Introduction**

39 Indirect observations of the atmosphere, ocean, and land surface conditions obtained using so-
40 phisticated satellite remote sensing instruments are an indispensable component of the global ob-
41 serving system. For numerical weather prediction (NWP) applications, satellite radiances from
42 visible, infrared, and microwave bands provide important information about atmospheric vari-
43 ables, such as temperature, winds, water vapor, and clouds, as well as lower boundary variables
44 such as soil moisture, vegetation biomass, and sea surface temperatures. Satellite observations can
45 also be used to detect the presence of aerosols and trace gases that are important for health and air
46 quality models. Recent enhancements to the global satellite observing system through deployment
47 of more accurate sensors onboard geostationary and polar-orbiting satellite platforms has made it
48 possible to routinely monitor environmental conditions with high spatial and temporal resolution
49 across the entire globe (Klaes et al. 2007; Strow 2013; Bessho et al. 2016; Schmit et al. 2017).

50 As satellite remote sensing capabilities have expanded and improved during the past several
51 decades, substantial progress has also been made in our ability to extract more information from
52 these important observations through development of advanced data assimilation (DA) methods
53 and more accurate NWP models. Despite using only a small percentage of all available observa-
54 tions, satellite brightness temperatures and derived products such as atmospheric motion vectors
55 still constitute more than 90% of the observations that are actively assimilated in most operational
56 global NWP models (Bauer et al. 2010). Satellite observations are especially important in data
57 sparse regions or for model state variables such as clouds and water vapor for which conventional
58 in situ observations with high spatial and temporal resolution are not available.

59 Until the past decade, however, almost all efforts within the operational and research DA com-
60 munities were directed toward optimizing the use of clear-sky brightness temperatures. This point

61 of emphasis was not made because cloud-impacted observations were deemed unimportant, but
62 rather, was due to the difficulty of using them in existing DA systems (Errico et al. 2007). Indeed,
63 until the recent development of all-sky DA methods, the need to exclude observations impacted
64 by clouds and precipitation meant that only a small percentage of available satellite observations
65 were actively assimilated at global NWP centers (Yang et al. 2016). This limitation is even more
66 severe for regional-scale NWP models where the entire domain may be covered by clouds (Lin et
67 al. 2017). Though more effective assimilation of clear-sky satellite brightness temperatures has
68 contributed to a steady increase in forecast skill, neglecting observations impacted by clouds is
69 problematic because they tend to be located in dynamically active regions where the generation of
70 more accurate initialization datasets through better use of these observations could help constrain
71 potentially rapid error growth in NWP models (McNally 2002).

72 Observations sensitive to clouds and precipitation are challenging to use for a variety of rea-
73 sons (Errico et al. 2007). For example, though observation-minus-background (OMB) departure
74 statistics are generally close to Gaussian for clear-sky observations, they can have substantial non-
75 Gaussian error characteristics in the presence of clouds and precipitation (Bocquet et al. 2010;
76 Okamoto et al. 2014; Harnisch et al. 2016; Otkin et al. 2018). Short-range model forecasts used
77 as the first guess often exhibit large errors in the placement and characteristics of clouds and pre-
78 cipitation. Limited predictability of small-scale features and the difficulty of accurately modeling
79 moist processes means that it is common for the model first guess to have much larger errors for
80 clouds and precipitation than it does for dynamical variables such as temperature and geopoten-
81 tial height (Fabry and Sun 2010). Though representativeness errors can usually be ignored when
82 assimilating clear-sky observations primarily sensitive to temperature, they become important for
83 cloud-affected observations because they can lead to very large OMB departures that hinder their
84 assimilation (Geer and Bauer 2011; Geer et al. 2012; Okamoto 2013). It is also more difficult to

85 quantify the observation and model background errors because it can be challenging to separate
86 signals associated with the individual atmospheric and land surface variables that contribute to the
87 sensitivity of a given satellite observation (Bauer et al. 2011). Another prominent problem is the
88 difficulty of modeling complex cloud properties in the radiative transfer models used to compute
89 the model-equivalent brightness temperatures. Nonlinear error characteristics due to deficiencies
90 in the radiative transfer and NWP models could lead to erroneous analysis increments in the model
91 state variables that in turn could impact balance and stability during the first few hours of the fore-
92 cast (Errico et al. 2007). Last, it is also important to account for correlated observation errors
93 because they can become very large in the presence of clouds and precipitation (Bormann et al.
94 2011, 2016; Campbell et al. 2017).

95 Despite these and other issues that make it challenging to assimilate cloud-sensitive observa-
96 tions, substantial progress has still been made during the past decade (Geer et al. 2017, 2018).
97 Successful efforts to assimilate all-sky satellite observations have occurred in tandem with im-
98 provements in the representation of water vapor and cloud features in NWP models and advances
99 in the ability of radiative transfer models to accurately model radiative fluxes in clouds. These
100 efforts have also been aided through the widespread adoption of four-dimensional variational
101 (4DVAR) and ensemble DA methods that can more easily extract information about dynamical
102 variables from cloud- and moisture-sensitive observations (Geer et al. 2014; Lien et al. 2016;
103 Zhu et al. 2016). For example, Peubey and McNally (2009) demonstrated that four-dimensional
104 variational methods could extract useful information about the wind field from moisture-sensitive
105 satellite observations through the "tracer-advection" mechanism. Likewise, ensemble DA systems
106 can infer the temperature, water vapor, and wind fields through ensemble covariances that link the
107 model state variables to the simulated observations (Zhang et al. 2011; Houtekamer and Zhang
108 2016). Compared to DA methods that only assimilate clear-sky satellite observations, an impor-

109 tant benefit of an all-sky DA approach is that it provides a unified treatment of cloud-free and
110 cloud-impacted observations that negates the need to perform potentially unreliable and expensive
111 cloud detection procedures (Bauer et al. 2010). An all-sky DA approach also promotes a more
112 balanced use of satellite observations in clear and cloudy areas that helps overcome the tendency
113 for operational DA systems to assimilate substantially more observations in regions that are not
114 affected by clouds or precipitation (Geer et al. 2017).

115 Early efforts to assimilate all-sky satellite observations focused on microwave sounding channels
116 that are sensitive to water vapor and non-precipitating cloud particles (Bauer et al. 2010). These
117 channels were initially chosen because they have more Gaussian error characteristics than cloud-
118 sensitive infrared and visible channels, thereby making them a logical starting point to explore the
119 assimilation of all-sky observations. Whereas it was once thought that it may prove too difficult
120 to assimilate water vapor and cloud-sensitive satellite observations (e.g., Bengtsson and Hodges,
121 2005), their impact has increased greatly in recent years (Geer et al. 2018). The direct assimilation
122 of all-sky microwave observations was first accomplished in an operational DA system in 2009 at
123 the European Centre for Medium-range Weather Forecasting (ECMWF) (Bauer et al. 2010). Since
124 then, the impact of these observations has risen to nearly 20% (Geer et al. 2017), as measured using
125 the forecast sensitivity observation impact metric (Langland and Baker 2004). This rapid increase
126 in their impact means that all-sky microwave observations have become one of the most important
127 sources of data in the ECMWF model, with an impact comparable to clear-sky satellite radiances
128 and conventional observations. More recently, the National Centers for Environmental Prediction
129 has also started to assimilate all-sky microwave observations in their operational global forecasting
130 system (Zhu et al. 2016). Numerous studies have documented the benefits of assimilating all-sky
131 microwave observations in global and regional modeling systems (e.g., Aonashi and Eito 2011;

132 Geer et al. 2014; Yang et al. 2016; Kazumori et al. 2016; Baordo and Geer 2016; Zhang and Guan
133 2017; Lawrence et al. 2018; Wu et al. 2019).

134 In contrast to the extensive resources that have been directed by the operational DA community
135 toward the assimilation of all-sky microwave observations, much less attention has been given to
136 increasing the use of cloud-sensitive infrared brightness temperatures. Indeed, until the past few
137 years, most studies that explored the assimilation of all-sky infrared observations have done so
138 using research models or within the context of observing system simulation experiments (OSSEs).
139 Early studies by Vukicevic et al. (2004, 2006) assimilated cloudy-sky infrared brightness tem-
140 peratures from the 10.7- and 12.0- μm bands on the Geostationary Operational Environmental
141 Satellite (GOES) Imager using a 4DVAR assimilation system. Observations from these atmo-
142 spheric window bands were shown to improve the depiction of upper-level ice clouds; however,
143 they had less impact on liquid clouds occurring lower in the troposphere. Subsequent studies by
144 Stengel et al. (2009, 2013) found that assimilation of cloud-impacted infrared observations from
145 the 6.2- and 7.3- μm water vapor channels on the Spinning Enhanced Visible and Infrared Imager
146 (SEVIRI) sensor led to more accurate analyses and forecasts in a high-resolution regional-scale
147 model. Other investigators proposed several methods that could be used to assimilate information
148 from cloud-impacted observations from hyperspectral sounders onboard polar-orbiting satellite
149 platforms (Heillette and Garand 2007; Pavelin et al. 2008; McNally 2009; Pangaud et al. 2009;
150 Guidard et al. 2011; Lupu and McNally 2012). All of these methods were designed to estimate
151 the cloud top pressure or effective cloud amount, with these parameters then fed to the DA system.
152 This process enabled the assimilation of some cloud information from these observations.

153 The direct assimilation of cloud and water vapor sensitive infrared brightness temperatures has
154 also been investigated using regional-scale OSSEs. Most of these studies employed ensemble DA
155 systems and were used to examine the potential impact of assimilating observations from the Ad-

156 vanced Baseline Imager (ABI) onboard the GOES-R satellite (currently GOES-16 and GOES-17).
157 In studies assimilating both clear- and cloudy-sky brightness temperatures from the ABI 8.5 μm
158 band, Otkin (2010, 2012a) showed that their assimilation improved the cloud field and that it was
159 necessary to use a short horizontal localization radius to account for small-scale cloud features
160 in the infrared observations. A subsequent study by Otkin (2012b) revealed that assimilation of
161 all-sky observations from the three water vapor sensitive bands on the ABI sensor had a large pos-
162 itive impact on 6-h precipitation forecasts during a high-impact winter storm. Jones et al. (2013a,
163 2014) examined the impact of simultaneously assimilating all-sky ABI brightness temperatures
164 and Doppler radar reflectivity observations for an extratropical cyclone, where it was found that
165 the most accurate analyses and forecasts were obtained when both observation types were assimi-
166 lated because they are sensitive to different portions of the cloud field. The radar observations had
167 a large positive impact on the cloud and wind fields in the lower troposphere, whereas the satel-
168 lite observations provided additional improvements in the cloud and moisture fields in the upper
169 troposphere. Other OSSE studies have shown similar positive results for various weather features,
170 such as mesoscale convective systems and tropical cyclones (Zupanski et al. 2011; Cintineo et al.
171 2016; Zhang et al. 2016; Minamide and Zhang 2017, 2018; Pan et al. 2018).

172 Results from the various OSSE studies have been used to inform ongoing efforts by various
173 groups to assimilate real all-sky infrared brightness temperatures and satellite-derived products.
174 Most of these studies have focused on optimizing methods to assimilate data from geostationary
175 satellite sensors in regional-scale ensemble DA systems. Geostationary satellite observations are
176 very useful for these models because they are the only source of cloud and water vapor informa-
177 tion with high spatial resolution. Moreover, unlike polar-orbiting satellites, geostationary sensors
178 are also able to provide frequent observation updates that cover most, if not all, of the model
179 domain. Some recent studies have shown positive results when assimilating satellite-derived prod-

180 ucts such as cloud water path or layer precipitable water (Jones et al. 2013b, 2015, 2016, 2018;
181 Schomburg et al. 2015; Jones and Stensrud 2015; Kerr et al. 2015; Wang et al. 2018), whereas
182 other studies have explored the direct assimilation of all-sky infrared brightness temperatures.
183 Regardless, there is great potential in assimilating all-sky observations from geostationary satel-
184 lite sensors in regional-scale models because clouds are the first observable aspect of convective
185 systems (Gustafsson et al. 2018; Kurzrock et al. 2019).

186 Okamoto (2013) showed a slightly positive impact on temperature and wind analyses and 6-
187 h forecasts when a subset of infrared brightness temperatures depicting spatially homogeneous
188 clouds in the middle and upper troposphere were assimilated. Subsequent studies by Okamoto et
189 al. (2014) and Harnisch et al. (2016) developed cloud-dependent all-sky observation error models
190 where the error is allowed to vary as a function of a diagnosed cloud impact parameter. Similar
191 in construct to the "symmetric" observation error model developed by Geer and Bauer (2011) for
192 all-sky microwave observations, both models assign the largest errors to the most strongly cloud-
193 impacted observations given greater uncertainties in both the NWP and radiative transfer models
194 in cloudy scenes. Minamide and Zhang (2017) have proposed an alternative method, known as
195 adaptive observation error inflation, that scales the observation errors as a function of the first guess
196 departure, with the largest errors given to observations with the largest departures. Application of
197 these dynamical observation error models to all-sky infrared brightness temperatures generally
198 leads to more Gaussian departure statistics, thereby promoting a more effective assimilation of
199 these observations.

200 Other studies have shown that assimilation of all-sky infrared observations from geostationary
201 satellite sensors can improve forecasts for tropical cyclones, floods, and severe thunderstorms
202 (Zhang et al. 2016, 2018; Honda et al. 2018a,b; Minamide and Zhang 2018). In particular, these
203 case studies revealed that assimilation of all-sky observations improved the prediction of the mid-

204 level mesocyclone during a tornadic thunderstorm and the structure of the inner core and outer
205 rainband regions for several tropical cyclones. More accurate precipitation forecasts were also
206 shown to lead to more skillful flood forecasts from a river discharge model (Honda et al. 2018b).
207 Though the direct assimilation of all-sky infrared brightness temperatures is currently not included
208 in any operational DA systems, Geer et al. (2019) present promising early results from a semi-
209 operational implementation of the ECMWF model. Their study assimilated all-sky observations
210 from seven water vapor sensitive bands on the Infrared Atmospheric Sounding Interferometer
211 sensor onboard the polar-orbiting Metop-A and Metop-B satellites. It was shown that the newly-
212 developed all-sky DA approach gave results that were as good or better than the existing clear-
213 sky-only approach, with the largest benefits found in the tropics where short-range forecasts were
214 improved throughout the troposphere and stratosphere.

215 In this study, we advance efforts to assimilate all-sky infrared brightness temperatures from
216 the cloud and water vapor sensitive $6.2\text{-}\mu\text{m}$ band on the SEVIRI sensor using a pre-operational
217 version of the Kilometer-scale Ensemble Data Assimilation (KENDA) system run at the German
218 Deutscher Wetterdienst (DWD). Experiments are run in which the nonlinear bias correction (NBC)
219 method developed by Otkin et al. (2018) is used to remove systematic biases from the all-sky ob-
220 servations prior to their assimilation. Given the proven utility of clear-sky satellite BC methods
221 (Eyre 2016), it is necessary to develop cloud-dependent BC methods for all-sky infrared brightness
222 temperatures to make full use of these observations within modern DA systems. Cloud-dependent
223 biases can occur for a variety of reasons. For example, deficiencies in the forward radiative trans-
224 fer model used to compute the model-equivalent brightness temperatures, or the inability of the
225 parameterization schemes in the NWP model to accurately represent the spatial extent, thickness,
226 and optical properties of clouds, can introduce systematic errors that vary as a nonlinear function
227 of some cloud property, such as cloud top height (Dee 2005; Dee and Uppala 2009; Mahfouf 2010;

228 Otkin and Greenwald 2008; Cintineo et al. 2014; Eikenberg et al. 2015). Though the accuracy
229 of radiative transfer models has improved greatly in recent years, there are still large uncertainties
230 regarding the specification of cloud properties, especially for ice clouds (Yang et al. 2013; Baum
231 et al. 2014; Yi et al. 2016).

232 Most BC methods use a set of predictors describing aspects of the atmospheric state or charac-
233 teristics of the satellite data to remove biases from the OMB departures (Eyre 2016). So-called
234 "static" BC methods use a set of departures accumulated over long periods of time outside of the
235 DA system to estimate and remove biases from the observations (Eyre 1992; Harris and Kelly
236 2001; Hilton et al. 2019). In contrast to the non-time-varying BC coefficients derived using static
237 methods, variational BC (VarBC) methods update the BC coefficients during each DA cycle using
238 an augmented control vector (Derber et al. 1991; Parrish and Derber 1992; Derber and Wu 1998;
239 Dee 2005; Auligne et al. 2007; Dee and Uppala 2009; Zhu et al. 2014, 2016). Recently, Zhu et al.
240 (2016) expanded an existing operational VarBC method so that it could be used to remove biases
241 from all-sky microwave observations. To reduce errors associated with mismatched cloud fields,
242 the BC coefficients with this method were computed using only situations where both the observed
243 and model-equivalent brightness temperatures were diagnosed as clear or cloudy. Though most
244 studies have focused on variational or hybrid DA systems, several studies have also explored their
245 use in ensemble DA systems (Szunyogh et al. 2008; Fertig et al. 2009; Stengel et al. 2009, 2013;
246 Miyoshi et al. 2010; Aravequia et al. 2011; Cintineo et al. 2016).

247 BC methods typically assume that a linear relationship exists between the OMB departure bias
248 and a given set of predictors. Though previous studies have shown that linear BC methods are
249 able to effectively remove biases from clear-sky satellite observations, these methods are subop-
250 timal if the observation bias varies as a nonlinear function of some predictor. Otkin et al. (2018)
251 showed that nonlinear conditional biases are more likely to occur for cloudy observations, which

252 necessitates development of BC methods that can more easily capture complex error patterns when
253 assimilating all-sky observations. Their study also showed that cloud-sensitive predictors, such as
254 cloud top height or the brightness temperatures themselves, are most effective at removing biases
255 from all-sky infrared observations. In this study, we build upon the work of Otkin et al. (2018) by
256 assessing the ability of linear and nonlinear BC predictors in the context of all-sky infrared bright-
257 ness temperature assimilation to improve short-range (1-h) forecasts in an ensemble DA system.
258 The paper is organized as follows. The DA framework is described in section 2, with assimilation
259 results using different linear and nonlinear BC predictors presented in section 3. Conclusions and
260 a discussion are presented in section 4.

261 **2. Experimental Design**

262 *a. SEVIRI Satellite Datasets*

263 The DA experiments performed during this study employed all-sky infrared brightness tempera-
264 tures from the SEVIRI sensor onboard the Meteosat Second Generation satellite, along with cloud
265 top height (CTH) retrievals provided by the EUMETSAT Nowcasting Satellite Applications Fa-
266 cility. The SEVIRI sensor observes the top-of-atmosphere radiances across 12 visible and infrared
267 spectral bands, with a nadir resolution of 3 km for all infrared bands (Schmetz et al. 2002). This
268 study focuses on the assimilation of clear and cloudy-sky brightness temperatures from the $6.2 \mu\text{m}$
269 band sensitive to clouds and water vapor in the upper troposphere. Under clear-sky conditions, the
270 weighting function for this band peaks near 350 hPa for a standard mid-latitude atmosphere; how-
271 ever, it will shift upward and become truncated near the cloud top when clouds are present due to
272 increased scattering. It will also peak at a higher (lower) atmospheric level if more (less) water
273 vapor is present in the middle and upper troposphere. The dual sensitivity of this band to clouds

274 and water vapor is advantageous for DA applications because increasing moisture and increasing
275 cloud optical thickness influence the infrared brightness temperatures in a similar way. The resul-
276 tant smoother dependence between water in its vapor and condensed (cloud) states will generally
277 lead to more Gaussian statistics than would occur with an infrared atmospheric window band that
278 has little or no sensitivity to water vapor.

279 As will be discussed in Section 3, CTH retrievals derived from SEVIRI observations were used
280 as one of the BC predictors during the DA experiments. With this dataset, the CTH is estimated for
281 each satellite pixel by first computing a simulated clear-sky $10.8 \mu\text{m}$ brightness temperature using
282 the Radiative Transfer for TOVS (RTTOV) radiative transfer model (Saunders et al. 1993) and
283 temperature and water vapor profiles from the global NWP model run at the DWD (Majewski et
284 al. 2002). An opaque cloud is then inserted in the atmospheric profile at successively higher levels
285 until the difference between the observed and simulated brightness temperatures is minimized
286 (Derrien and Le Gleau 2005). The CTH retrievals have a nominal vertical resolution of 200 m;
287 however, their uncertainty is larger for semi-transparent clouds (Le Gleau 2016). To minimize
288 the impact associated with spatially correlated errors, the CTH retrievals and SEVIRI brightness
289 temperatures were horizontally thinned by a factor of five in the meridional and zonal directions.
290 This reduces their horizontal resolution to $\sim 20\text{-}25$ km across the model domain, which is ~ 8 times
291 coarser than the resolution of the NWP model employed during this study.

292 *b. KENDA Data Assimilation System*

293 Ensemble DA experiments were performed using a research version of the KENDA system
294 (Schraff et al. 2016) used at the DWD. A major development focus of KENDA in recent years has
295 been the inclusion of cloud- and precipitation-sensitive observations that can be used to constrain
296 the cloud and thermodynamic fields in convection-resolving models. KENDA employs a local

297 ensemble transform Kalman filter (Hunt et al. 2007) during the analysis step and the Consortium
298 for Small-scale Modeling (COSMO) NWP model (Baldauf et al. 2011) during the forecast step.
299 All of the DA experiments were run on the COSMO-DE domain covering Germany and parts
300 of surrounding countries with 2.8 km horizontal resolution. With this version of KENDA, the
301 lateral boundary conditions were obtained at hourly intervals from the COSMO-EU domain run
302 at the DWD, which in turn was driven by lateral boundary conditions from the global Icosahedral
303 non-hydrostatic (ICON) model (Zangl et al. 2015). The COSMO-DE domain contains 50 terrain-
304 following vertical layers, with the model top located near 22 km (about 40 hPa).

305 The COSMO model includes prognostic variables for atmospheric temperature, pressure, hor-
306 izontal and meridional wind components, and the mixing ratios for water vapor, cloud water,
307 rainwater, ice, snow, and graupel. Cloud microphysical processes are handled using a simplified
308 version of the double-moment Seifert and Beheng (2001) microphysics scheme that was reduced
309 to a single-moment scheme for computational purposes, whereas the parameterization of cloud
310 formation and decay processes is based on Lin et al. (1983). Though deep convection is explicitly
311 resolved on the COSMO-DE domain, a simplified version of the Tiedtke (1989) mass-flux scheme
312 is used to parameterize shallow convection. Atmospheric turbulence is predicted using the 2.5
313 order turbulent kinetic energy scheme developed by Raschendorfer (2001). A δ -2 stream radia-
314 tive transfer method is used to update atmospheric heating rates due to radiative effects at 15-min
315 intervals (Ritter and Geleyn 1992).

316 The DA experiments employed a 40-member ensemble, along with a deterministic run that is
317 initialized by applying the Kalman gain matrix from the assimilation update to the deterministic
318 model background. The ensemble and deterministic runs were initialized at 00 UTC on 28 May
319 2014 and then updated at hourly intervals during a 3-day period. Model-equivalent brightness
320 temperatures for the SEVIRI 6.2 μm band were computed using version 10.2 of the RTTOV

321 radiative transfer model that includes an enhanced cloud-scattering module that enables the use
322 of cloud hydrometeor profiles located on the NWP model vertical grid (Matricardi 2005; Hocking
323 et al. 2011). Vertical profiles of fractional cloud cover and ice and liquid water contents used to
324 compute the cloudy-sky brightness temperatures were obtained using COSMO model output and
325 empirical relationships developed by Kostka et al. (2014). The maximum-random cloud overlap
326 scheme (Raisanen 1998) was used, with the ice crystals assumed to have a hexagonal shape and
327 the effective particle diameters computed using the McFarquhar et al. (2003) method.

328 SEVIRI $6.2 \mu\text{m}$ brightness temperatures, along with radiosonde, surface, wind profiler, and air-
329 craft observations, were actively assimilated at hourly intervals during each DA experiment. The
330 corresponding model equivalents were computed at the exact observation times through inclusion
331 of the various observation operators within the COSMO model. Covariance inflation values were
332 computed at each grid point using a combination of the relaxation to prior perturbations approach
333 described by Zhang et al. (2004) and multiplicative inflation based on Anderson and Anderson
334 (1999). Covariance localization was performed by using only those observations located within
335 a specified horizontal radius of a given analysis point. An adaptive horizontal localization radius
336 was used for the conventional observations (Perianez et al. 2014); however, it was set to 35 km
337 for the all-sky SEVIRI brightness temperatures given their uniform data coverage. The vertical
338 localization scale was set to 0.7 in logarithm of pressure for the brightness temperatures, with the
339 localization height determined using the peak of the satellite weighting function for the simulated
340 brightness temperature from the deterministic run. The observation error was set to 4 K for the
341 all-sky brightness temperatures, similar to that used in Otkin (2012b) and Cintineo et al. (2016).
342 Though it may have been advantageous to use a cloud-dependent observation error model, that is
343 beyond the scope of the current study.

344 *c. Nonlinear Bias Correction Method*

345 Systematic biases were removed from the satellite observations using the NBC method devel-
346 oped by Otkin et al. (2018). This method uses a Taylor series polynomial expansion of the OMB
347 departures for a given satellite band to remove linear and nonlinear conditional biases from the
348 observations prior to their assimilation. A brief overview of the NBC method is provided here,
349 with the reader referred to Otkin et al. (2018) for a more detailed description. To begin, the OMB
350 departure vector is defined as:

$$d\mathbf{y} = \mathbf{y} - H(\mathbf{x}), \quad (1)$$

351 where \mathbf{y} and $H(\mathbf{x})$ are vectors containing the observed and model-equivalent brightness tempera-
352 tures, respectively, and H is the observation operator that is used to convert the NWP model first
353 guess fields into simulated brightness temperatures. If we assume that any biases present in the
354 OMB departures can be described by a real function $f(z)$ that is infinitely differentiable around
355 a real number c , Eqn. 1 can be decomposed into an N order Taylor series polynomial expansion.
356 A representative example in which a single predictor is used to identify biases in a given set of
357 observations using a 3rd order expansion is shown in Eqn. 2:

$$d\mathbf{y} = \left(b_0 + b_1(z^{(i)} - c) + b_2(z^{(i)} - c)^2 + b_3(z^{(i)} - c)^3 \right)_{i=1,\dots,m} \quad (2)$$

358 where m is the number of observations, $z(i)$ is the predictor value for the i th observation, b_n are
359 the 0... n th BC coefficients, and c is a constant that can be set to any value. The $(i = 1, \dots, m)$
360 notation outside the parentheses indicates that the Taylor series terms are computed separately for
361 each element of the observation departure vector. In this example, the first two terms on the right
362 hand side represent the constant and linear bias components, whereas the last two terms represent
363 the nonlinear 2nd order (quadratic) and 3rd order (cubic) components.

Eqn. 2 can be rewritten in matrix notation as $d\mathbf{y} = \mathbf{A}\mathbf{b}$, where \mathbf{A} is an $m \times n$ matrix containing the n Taylor series terms for each observation and \mathbf{b} is an $n \times 1$ vector containing the BC coefficients. This is an overdetermined system of m linear equations in n unknown coefficients because $m > n$. The BC coefficients that best fit the set of equations can be identified by solving the quadratic minimization problem, which, after adding a Tikhonov regularization term (αI) to improve its conditioning, leads to:

$$\mathbf{b} = (\alpha I + \mathbf{A}^T \mathbf{A})^{-1} \mathbf{A}^T d\mathbf{y} \quad (3)$$

The $(\alpha I + \mathbf{A}^T \mathbf{A})$ matrix is a symmetric, $n \times n$ square matrix, thereby making it easy to compute its inverse. The Tikhonov regularization term is defined to be a multiple of the identity matrix, which is a standard approach when solving inverse problems (Nakamura and Potthast 2015). The constant α was set to a very small value (10^{-9}) following the results of Otkin et al. (2018).

For this study, the BC coefficients for the SEVIRI $6.2 \mu\text{m}$ band were updated during each assimilation cycle using only the observation departure statistics accumulated during the previous hour. This approach was used rather than accumulating statistics over a longer time period because it allows the BC coefficients to quickly adapt to changes in the cloud field, such as those associated with the diurnal cycle of convection and its impact on cloud properties in the upper troposphere. All of the observation departures for a given assimilation cycle were used to compute the BC coefficients, thereby providing a larger sample size and negating the need to identify cloud-matched observations. After computing the BC coefficients, they were then applied separately to each observation and ensemble member.

3. Results

In this section, we assess the ability of all-sky infrared brightness temperatures from the SEVIRI $6.2 \mu\text{m}$ band to improve short-range forecasts when assimilated in an ensemble DA system after

386 using various BC predictors to remove biases from the observations. Figure 1 shows the evolution
387 of the upper-level cloud and water vapor fields during the 3-day assimilation period, as depicted by
388 the SEVIRI 6.2 μm brightness temperatures. At the start of the period, an extensive area of cold,
389 upper-level clouds associated with widespread precipitation extended from northwest-to-southeast
390 across the domain (Fig. 1a). As this weather feature slowly moved toward the south and weakened
391 during the next two and a half days, the lower brightness temperatures indicative of optically thick
392 clouds were steadily replaced by higher brightness temperatures as the clouds became optically
393 thinner and their spatial extent lessened. A small area of clear skies across the southwestern part
394 of the domain was shunted southward during this time period, and was replaced by a much larger
395 area of clear skies behind the departing weather feature (Fig. 1e). Within these clear-sky areas, the
396 highest brightness temperatures are associated with the driest conditions in the upper troposphere.
397 Overall, this synopsis shows that there were a wide range of cloud and water vapor conditions in
398 the upper troposphere that together support a realistic assessment of the impacts of the infrared
399 observations and bias predictors on the performance of the assimilation system.

400 *a. Assessing the Impact of Nonlinear Bias Corrections*

401 Prior work by Otkin et al. (2018) found that it was necessary to use nonlinear BC predictors
402 to remove cloud-dependent biases from passively monitored all-sky infrared brightness tempera-
403 tures. Here, we extend their results by examining the impact of nonlinear BC predictors in cycled
404 DA experiments where all-sky 6.2 μm brightness temperatures are actively assimilated. In par-
405 ticular, experiments are performed where the observation bias is removed using a 0th (constant),
406 1st (linear), 2nd (quadratic), or 3rd (cubic) order Taylor series polynomial expansion of the OMB
407 departures when the observed cloud top height is used as the bias predictor. To provide complete
408 domain coverage, satellite pixels identified as clear in the EUMETSAT cloud top height product

409 were assigned a height equal to the model terrain elevation. These four experiments are hereafter
410 referred to as OBSCTH-0TH, OBSCTH-1ST, OBSCTH-2ND, and OBSCTH-3RD, respectively.
411 Results from these experiments are then compared to two baseline experiments in which the all-
412 sky infrared observations are either not assimilated (No-Assim), or are actively assimilated, but
413 without using any bias corrections (No-BC). The impact of the BC predictors is assessed using
414 OMB departure statistics from the prior ensemble mean analyses accumulated at hourly intervals
415 during the 72-h assimilation period. The prior analyses are used here to provide a measure of the
416 observation impact on short-range (1-h) forecasts.

417 1) BRIGHTNESS TEMPERATURE BIAS CORRECTION STATISTICS

418 To assess how the BC changes in relation to use of linear and nonlinear predictors, Fig. 2 shows
419 the 2-D probability distribution of OMB departures for the $6.2 \mu\text{m}$ brightness temperatures from
420 the No-Assim experiment (Fig. 2a), along with the corresponding BC distributions for each DA
421 experiment. All of the distributions are plotted as a function of the observed $6.2 \mu\text{m}$ brightness
422 temperatures. The magenta line in each panel denotes the mean of the entire distribution, whereas
423 the shorter black lines depict the conditional mean in each column. Inspection of Fig. 2a re-
424 veals that, though the mean bias during the No-Assim experiment is relatively small (-0.76 K), the
425 conditional biases exhibit an asymmetrical arch-shaped pattern that is a nonlinear function of the
426 observed brightness temperatures. The conditional biases are close to zero for brightness temper-
427 atures near 235 K , and remain small for brightness temperatures $> 230 \text{ K}$; however, they become
428 progressively more negative for lower brightness temperatures. The large negative biases for the
429 lowest brightness temperatures indicate that the COSMO model forecasts are deficient in upper-
430 level clouds or that there are biases in the RTTOV model used to compute the model-equivalent
431 brightness temperatures. Regardless, assimilation of observations with such large biases could

432 degrade the performance of the DA system. The simplest option is to exclude these observations,
433 however, that is not ideal because they still contain useful information about random errors in the
434 cloud field if the biases can be removed.

435 Inspection of the corrections applied to the infrared observations during the active DA experi-
436 ments (Figs. 2b-e) reveals that the mean BC is similar for all experiments despite the 2-D distribu-
437 tions having very different shapes. This occurs because the mean BC is most strongly influenced
438 by the mean bias in the full set of OMB departures (Fig. 2a) and by the tendency for larger cor-
439 rections for the lower brightness temperatures to be offset by smaller corrections for the higher
440 brightness temperatures. Because the single bias predictor in the OBSCTH-0TH experiment (Fig.
441 2b) is only able to remove the mean bias during a given assimilation cycle, it has a narrower BC
442 distribution than the other experiments. There is still some spread in the corrections during this
443 experiment because the mean BC varies with time due to changes in the prevailing atmospheric
444 conditions. The constant corrections, however, are not optimal because they are unable to account
445 for the large variations in the conditional biases across the OMB distribution (Fig. 2a). In contrast,
446 more accurate corrections are obtained through application of the linear bias predictor during the
447 OBSCTH-1ST experiment (Fig. 2c), as evidenced by the smaller (larger) BC for brightness tem-
448 peratures greater (less) than 230 K. The corrections for the lower brightness temperatures become
449 even larger during the OBSCTH-2ND and OBSCTH-3RD experiments (Fig. 2d, e) because the
450 additional nonlinear predictors are able to remove more of the conditional biases at those tem-
451 peratures (Fig. 2a). Overall, these results indicate that the OBSCTH-2ND and OBSCTH-3RD
452 experiments provide more accurate BC in the presence of complex nonlinear bias patterns.

453 2) BRIGHTNESS TEMPERATURE ERROR TIME SERIES

454 The evolution of the $6.2 \mu\text{m}$ brightness temperature root mean square error (RMSE) and bias
455 during the 3-day assimilation period is shown in Fig. 3. The error statistics are computed using
456 the ensemble mean brightness temperatures from the prior analyses for each assimilation cycle.
457 Note that the bias is nonzero for all of the experiments because the statistics are computed using
458 output from 1-h forecasts and prior to bias-correcting the satellite observations. Overall, there is
459 a large diurnal cycle in the error statistics, with the largest RMSE and negative biases occurring
460 during the daytime (09-18 UTC), followed by smaller errors at night. This error pattern is con-
461 sistent with a lack of lower brightness temperatures during the afternoon when the deficiency in
462 upper-level clouds associated with deep convection is most prominent (not shown). The large di-
463 urnal differences in the bias also illustrate why it is advantageous to compute the BC coefficients
464 using observations from a single assimilation cycle because accumulation of OMB departures over
465 longer time periods would obscure these important differences and therefore make the BC method
466 less effective.

467 Inspection of the error time series reveals that the bias and RMSE are smallest during the No-BC
468 experiment, which indicates that larger improvements are realized in the forecast cloud field when
469 BC is not applied to the all-sky brightness temperatures. As will be shown in the next section, how-
470 ever, the improved fits to the satellite observations during the No-BC experiment do not translate
471 into smaller errors for conventional observations that are not sensitive to clouds. Compared to the
472 No-Assim experiment, the four experiments in which bias-corrected satellite observations were
473 assimilated had similar biases, but much smaller RMSE, with values approaching those obtained
474 during the No-BC experiment. The simultaneous large reductions in RMSE and small changes
475 in bias demonstrate that even though the bias-corrected observations are unable to substantially

476 reduce the bias, it is still possible to use them to fix random errors in the cloud and water vapor
477 fields. Moreover, though there is a trend toward lower RMSE in all of the experiments during the
478 3-day assimilation period due to a decrease in upper-level clouds (Fig. 1), this decrease in RMSE
479 is larger for the experiments where infrared observations are assimilated. This result provides fur-
480 ther evidence that the all-sky infrared brightness temperatures are able to improve the cloud field
481 in the 1-h forecasts regardless of whether or not BC is applied to them prior to their assimilation.

482 3) CONVENTIONAL OBSERVATION ERROR ANALYSIS

483 To assess the impact of the nonlinear bias predictors on the thermodynamic and kinematic fields,
484 Fig. 4 shows vertical profiles of RMSE for air temperature, relative humidity, and the zonal and
485 meridional wind components computed using radiosonde observations accumulated over the 3-day
486 assimilation period and binned into 100 hPa layers. For each variable, RMSE profiles are shown
487 for the two baseline experiments (No-Assim and No-BC), followed by vertical profiles showing
488 the percentage changes in RMSE for the remaining experiments computed with respect to each of
489 the baseline experiments. This approach was used to make it easier to assess the impact of the bias
490 predictors, while still being able to show the baseline error profiles. Negative (positive) changes
491 mean that assimilation of the all-sky infrared observations decreased (increased) the errors relative
492 to a given baseline experiment and therefore improved (degraded) the prior analysis fits to the
493 radiosonde observations. Figure 5 shows the corresponding profiles of observation bias for each
494 experiment. Only raw error profiles are shown for this metric because small biases in the baseline
495 experiments make the percentage changes difficult to evaluate.

496 Comparison of the temperature RMSE profiles for the baseline experiments reveals that the
497 errors are up to 2% smaller (larger) in the upper (lower) troposphere when the all-sky observations
498 are assimilated during the No-BC experiment (Fig. 4b). The RMSE and bias for the radiosonde

499 temperatures were smaller below 400 hPa when the brightness temperature biases were removed
500 during the OBSCTH experiments; however, the errors increased by several percent above this
501 level (Fig. 4c, 5a). Because the largest BC is generally applied to lower brightness temperatures
502 associated with clouds in the upper troposphere (e.g., Fig. 2), the larger errors near and above
503 the tropopause indicate that removal of the brightness temperature bias may actually lead to some
504 degradation in the fits to the radiosonde temperatures. The larger temperature errors occur during
505 all of the OBSCTH experiments, however, which suggests that they may be related to removal of
506 the mean brightness temperature bias rather than to removal of the conditional biases. It is also
507 possible that some of the cloud and water vapor information from the all-sky satellite observations
508 is being incorrectly aliased onto the temperature field. Further work is necessary to identify the
509 cause of the larger temperature errors between 300 and 100 hPa.

510 For the relative humidity observations, the RMSE from the baseline experiments is relatively
511 small near the surface, but increases rapidly to over 20% by 800 hPa. It then remains large in
512 the middle troposphere before slowly decreasing with height in the upper troposphere (Fig. 4d).
513 The bias profiles from the baseline experiments likewise indicate that the model background is
514 too dry below 800 hPa, but too moist above this level (Fig. 5b). When all-sky brightness tem-
515 peratures are assimilated during the No-BC experiment, the RMSE increases throughout most of
516 the vertical profile (Fig. 4e), and the negative biases become even larger in the upper troposphere
517 (Fig. 5b). Indeed, the relative humidity errors are larger in the No-BC experiment than they are
518 in the No-Assim experiment despite the fact that the infrared observations are strongly sensitive
519 to water vapor in the upper troposphere. As discussed previously, the negative conditional biases
520 for brightness temperatures < 230 K indicate that the model background is deficient in upper level
521 clouds (Fig. 2a). Thus, it appears that trying to add clouds more forcefully through assimilation
522 of the non-bias-corrected observations leads to an incorrect aliasing of cloud information onto the

523 water vapor field. Instead of increasing the cloud condensate in response to the negative OMB
524 departures, the assimilation instead adds more water vapor to the model analyses. In contrast, both
525 the RMSE and bias are greatly reduced when BC is applied to the infrared observations during
526 the OBSCTH experiments (Fig. 4f, 5b). When combined with the brightness temperature statis-
527 tics shown in Fig. 3, this demonstrate that bias-correcting the all-sky infrared observations retains
528 some cloud information during the assimilation while also improving the water vapor field.

529 For the zonal and meridional wind observations, the RMSE profiles from the baseline exper-
530 iments have a sinusoidal appearance characterized by the largest errors in the lower and upper
531 troposphere and smaller errors in the mid-troposphere (Fig. 4g, k). The biases in the baseline ex-
532 periments are generally $< 0.2 \text{ m s}^{-1}$, with the largest biases occurring near 600 and 700 hPa for the
533 zonal and meridional wind components, respectively (Fig. 5c, d). The RMSE generally increases,
534 especially for the meridional wind component, when the satellite observations are assimilated dur-
535 ing the No-BC experiment (Fig. 4h, k). The wind errors are slightly reduced, however, when BC is
536 applied to the infrared brightness temperatures during the OBSCTH experiments (Fig. 4i, l). Even
537 so, it is evident that assimilation of the all-sky observations leads to a slightly negative impact on
538 the mid-tropospheric winds and only a neutral to slightly positive impact in the lower troposphere
539 and near the tropopause.

540 To more clearly assess the impact of the nonlinear BC predictors on each variable, summary
541 statistics were computed using all of the radiosonde observations during the 72-h assimilation
542 period. Table 1 shows the percentage changes in RMSE and bias for each OBSCTH experiment
543 relative to the No-BC experiment. Overall, it is evident that bias-correcting the infrared brightness
544 temperatures improves the quality of the model background fields. The largest improvements
545 (negative values) occur for the relative humidity field, with the bias reduced by at least 25% during
546 each experiment. Smaller improvements occurred for the other variables. Comparison of the

547 OBSCTH experiments reveals that there is a distinct advantage to using higher order nonlinear BC
548 terms to remove the bias from the all-sky brightness temperatures. For example, the RMSE for
549 the relative humidity and wind observations steadily decrease as the BC predictor increases from
550 the 0th (OBSCTH-0TH) to 3rd (OBSCTH-3RD) order. The impact of the higher order BC terms
551 is less consistent for temperature and for the relative humidity bias; however, the errors are still
552 smaller than occurred during the No-BC experiment. Together, the results presented in this section
553 have shown that it is necessary to bias correct the infrared observations prior to their assimilation
554 and that it is generally beneficial to include nonlinear BC predictors. This was demonstrated by
555 the tendency for the higher order predictors to have a neutral-to-positive impact on the temperature
556 and wind fields, while also improving the cloud and water vapor fields.

557 *b. Assessing the Impact of Different Bias Predictor Variables*

558 In this section, we assess the ability of individual bias predictor variables sensitive to clouds
559 and water vapor, or that depict variations in the satellite zenith angle, to improve the assimilation
560 of all-sky infrared brightness temperatures during cycled DA experiments. Based on results from
561 the previous section, all of the experiments employed a 3rd order polynomial expansion of the
562 OMB departures to remove biases from the satellite brightness temperatures prior to their assimi-
563 lation. In addition to the OBSCTH-3RD experiment presented in Section 3a (hereafter referred to
564 as BC-OBSCTH), experiments were performed in which the observed SEVIRI 6.2 μm brightness
565 temperatures (BC-OBSBT), satellite zenith angle (BC-SATZEN), or 100-700 hPa integrated water
566 content (BC-IWC) were used as the bias predictors. The integrated water content predictor was
567 calculated by converting the water vapor and all cloud hydrometeor mixing ratios in each model
568 layer into millimeters and then integrating over the 100-700 hPa layer. Together, these four predic-
569 tors were chosen because they were also used during the passive monitoring experiments presented

570 in Otkin et al. (2018). Here, we extend the results of that study by assessing the performance of
 571 these bias predictor variables when they are used during active DA experiments.

572 1) OBSERVATION SPACE DIAGNOSTICS

573 Figure 6 shows the evolution of the SEVIRI 6.2 μm brightness temperature bias, RMSE, ensem-
 574 ble spread, and consistency ratio (CR) for each experiment during the 3-day assimilation period.
 575 The statistics were computed for each assimilation cycle using brightness temperatures from the
 576 prior ensemble analyses. The ensemble spread is defined as:

$$\text{Spread} = \sqrt{\left\langle \frac{1}{N-1} \sum_{n=1}^N \left[H(\mathbf{x}_n) - \overline{H(\mathbf{x}_n)} \right]^2 \right\rangle}, \quad (4)$$

577 where N is the ensemble size, n is the index of a given ensemble member, and H is the observation
 578 operator (e.g., RTTOV) used to compute the model-equivalent brightness temperatures. The total
 579 ensemble spread is the combination of the observation error (σ_{obs} , set to 4 K) and ensemble spread,
 580 such that:

$$\text{Total Spread} = \sqrt{\sigma_{obs}^2 + \left\langle \frac{1}{N-1} \sum_{n=1}^N \left[H(\mathbf{x}_n) - \overline{H(\mathbf{x}_n)} \right]^2 \right\rangle}, \quad (5)$$

581 Finally, the RMSE and total spread are used to calculate the CR, which provides another diagnostic
 582 measure of the performance of the assimilation system:

$$\text{CR} = (\text{Total Spread})^2 / (\text{RMSE})^2 \quad (6)$$

583 With the CR, a value of 1 is desired because, in an ideal situation, the total spread should equal
 584 the RMSE for each observation type being assimilated. Values greater (less) than 1 indicate that
 585 there is too little (too much) ensemble spread and/or that the observation error is larger (smaller)
 586 than necessary (Dowell et al. 2004; Aksoy et al. 2009).

587 Inspection of the time series shows that the smallest RMSE and bias (Fig. 6a,b) occurred during
 588 the No-BC experiment, which is not surprising because assimilating non-bias-corrected obser-

589 vations should lead to the largest impact when assessed against themselves. Comparison of the
590 BC experiments reveals that the BC-SATZEN and BC-IWC experiments have larger biases and
591 RMSEs than the BC-OBSBT and BC-OBSCTH experiments. The larger positive impact of the
592 OBSBT and OBSCTH predictors on these two metrics is consistent with Otkin et al. (2018), who
593 showed that variables sensitive to the cloud top height are more effective at identifying biases in
594 all-sky infrared brightness temperatures. The results shown here indicate that using these predic-
595 tors in active DA experiments also leads to smaller errors in the cloud and water vapor fields in the
596 prior ensemble analyses when assessed using satellite observations.

597 The ensemble spread (Fig. 6c) generally decreases during the assimilation period due to a tran-
598 sition toward clearer skies and the cumulative impact of the all-sky brightness temperatures on the
599 cloud and water vapor fields. The decrease in ensemble spread is accompanied by a corresponding
600 increase in the CR (Fig. 6d), which peaks each day when the RMSE reaches its diurnal minimum.
601 Because the RMSE is smallest during the No-BC, BC-OBSCTH, and BC-OBSBT experiments
602 (Fig. 6b), they also have the largest CRs. The large CR values during all of the active DA experi-
603 ments reveal that it was sub-optimal to employ the same observation error variance for both clear
604 and cloudy-sky observations during the entire assimilation period. Thus, combining an adaptive
605 all-sky observation error model with the BC method would be beneficial; however, that is left for
606 future work. In addition, inspection of rank histograms for each experiment (not shown) revealed
607 that the ensemble spread is too small. This result points toward the need to also develop methods
608 that increase the ensemble spread in cloud hydrometeors because they have the largest impact on
609 the spread in the all-sky infrared brightness temperatures. One potential option would be to use
610 the stochastic parameter perturbations method (Berner et al. 2017) to add perturbations to cloud
611 source/sink terms to account for some of the uncertainty in cloud microphysics schemes. This has
612 been shown to increase the spread in cloudy regions (Griffin et al. 2019).

613 2) BRIGHTNESS TEMPERATURE BIAS CORRECTION STATISTICS

614 To further assess the behavior of each bias predictor, 2-D probability distributions of the ensemble mean BCs accumulated at hourly intervals during the 72-h assimilation period are shown for 615 each experiment in Fig. 7. Overall, the BC-OBSBT and BC-OBSCTH experiments have similar 616 distributions characterized by relatively small mean BCs for brightness temperatures > 230 K and 617 then a strong upward trend in the mean BC for lower brightness temperatures (Fig. 7a,b). Even 618 so, there are notable differences between these experiments, such as the larger BC for the lowest 619 brightness temperatures in the BC-OBSBT experiment and the wider vertical distribution for most 620 brightness temperatures in the BC-OBSCTH experiment. The BC patterns for both experiments 621 are flipped compared to the OMB departure distribution from the No-Assim experiment (Fig. 2a), 622 which is good because that means that the OBSBT and OBSCTH predictors are able to account 623 for the nonlinear, cloud-dependent conditional biases in that distribution. In contrast, the BC-IWC 624 and BC-SATZEN experiments have much smaller BCs for the lowest brightness temperatures that 625 then become larger for higher brightness temperatures. The mean BC is also larger during these 626 experiments, which indicates that the IWC and SATZEN predictors did not have the same positive 627 impact on the cloud field as the OBSBT and OBSCTH predictors. This behavior is consistent 628 with the brightness temperature bias time series shown in Fig. 6a, and provides further evidence 629 that it is necessary to use BC predictors sensitive to the cloud top height when assimilating all-sky 630 infrared brightness temperatures. 631

632 3) BRIGHTNESS TEMPERATURE INNOVATIONS

633 Next, we examine the $6.2 \mu\text{m}$ brightness temperature innovations during each experiment using 634 the 2-D probability distributions shown in Fig. 8. These distributions were constructed using the 635 ensemble mean innovations accumulated at hourly intervals during the 72-h assimilation period.

636 Inspection of Fig. 8a shows that the conditional mean innovations are close to zero across the
637 entire distribution during the No-Assim experiment. This indicates that the conventional in-situ
638 observations by themselves do not have a systematic impact on the cloud and water vapor fields
639 in the upper troposphere. During the No-BC experiment (Fig. 8b), the innovation pattern is very
640 similar to the OMB departure distribution in the No-Assim experiment (Fig. 2a), with large (small)
641 innovations occurring for lower (higher) brightness temperatures. This shows that the large condi-
642 tional biases for the lower brightness temperatures are strongly corrected during this experiment,
643 which is not surprising because BC was not applied to the brightness temperatures prior to their
644 assimilation. A similar pattern emerges during the BC-IWC and BC-SATZEN experiments (Fig.
645 8e, f) because their smaller BCs for lower brightness temperatures (Fig. 7c, d) meant that large in-
646 novations were still possible during each assimilation cycle. In contrast, the mean innovations are
647 very small across most of the distribution during the BC-OBSBT experiment (Fig. 8c) because the
648 larger BCs for lower brightness temperatures (Fig. 7a) reduces the size of the resultant innovations.
649 The distribution for the BC-OBSCTH experiment (Fig. 8d) has some larger negative innovations
650 for the lower brightness temperatures, but is otherwise similar to the BC-OBSBT experiment. The
651 smaller innovations during the BC-OBSBT and BC-OBSCTH experiments were likely beneficial
652 because they limited potential imbalances in the model due to large analysis increments, while still
653 leading to large reductions in the RMSE and bias (Fig. 6a, b).

654 4) CONVENTIONAL ERROR ANALYSIS

655 Finally, we examine the impact of the infrared brightness temperatures and BC predictors on
656 the accuracy of the prior ensemble mean analyses using OMB departure statistics accumulated
657 during the 72-h assimilation period for the radiosonde temperature, relative humidity, and zonal
658 and meridional wind observations. Figure 9 shows vertical profiles of RMSE for the No-Assim and

659 No-BC experiments, along with percentage changes in RMSE for each BC experiment, whereas
660 Fig. 10 shows the corresponding bias profiles. Summary statistics showing the percentage changes
661 in RMSE and bias during each BC experiment relative to the No-Assim and No-BC experiments
662 are shown in Tables 2 and 3, respectively.

663 Compared to the No-Assim experiment, the zonal and meridional wind speed errors in aggregate
664 are slightly smaller during the BC-OBSBT and BC-OBSCTH experiments, but increase by 0.5 –
665 0.8% during the BC-SATZEN and BC-IWC experiments (Table 2). Inspection of the zonal wind
666 profiles (Fig. 9h, i) shows that the overall smaller RMSE during the BC-OBSBT and BC-OBSCTH
667 experiments are primarily due to larger improvements in the upper and lower troposphere, with
668 some degradation evident in the mid-troposphere. Both of these experiments also have the smallest
669 meridional wind speed errors for most of the vertical layers (Fig. 9k, l). Indeed, the RMSE for
670 the meridional wind speed observations is 1.4% and 0.8% smaller during the BC-OBSBT and BC-
671 OBSCTH experiments, respectively, compared to a neutral impact when the IWC and SATZEN
672 predictors are used (Table 3).

673 Assimilation of the infrared brightness temperatures led to very different impacts on the RMSE
674 and bias for the radiosonde temperature observations. For example, though the RMSE in each
675 experiment increased by 0.8 – 1.0% relative to the No-Assim experiment, the bias was substan-
676 tially lower, with decreases ranging from -1.7% during the No-BC experiment to -6.1% for the
677 BC-SATZEN experiment (Table 2). Overall, the smallest biases are obtained during the various
678 BC experiments, with all but BC-SATZEN also having slightly smaller RMSEs than the No-BC
679 experiment (Table 3). Comparison of the vertical profiles shows that the temperature RMSEs are
680 smaller within most of the troposphere during the BC experiments (Fig. 9c); however, the presence
681 of much larger errors near the tropopause led to only a neutral to slightly positive impact when all
682 of the temperature observations are considered (Table 3).

683 For relative humidity, assimilating the infrared brightness temperatures without first removing
684 their biases led to sharply higher bias (30.1%) and RMSE (0.8%) during the No-BC experiment
685 (Table 2). In contrast, the overall RMSE and bias are much smaller during the other experiments
686 regardless of which BC predictor is used (Table 3). Compared to the No-BC experiment, the largest
687 RMSE reductions occur during the BC-OBSCTH (-1.8%) and BC-SATZEN (-1.4%) experiments,
688 with the largest bias reductions occurring during the BC-IWC (-45.2%), BC-SATZEN (-38.2%),
689 and BC-OBSCTH (-30.2%) experiments. The error profiles in Fig. 9f show that, though there
690 are some differences between the BC experiments, that the RMSEs are smaller in most of the
691 troposphere relative to the No-BC experiment. The biases are also greatly reduced in the middle
692 and upper troposphere (Fig. 10b).

693 In summary, the results presented in this section show that assimilation of infrared brightness
694 temperatures that are not bias-corrected leads to larger errors for all metrics, except for the tem-
695 perature bias, relative to the No-Assim experiment. Removal of the brightness temperature biases,
696 however, greatly improves the impact of the satellite observations, with the largest percentage
697 decreases in the errors realized for the relative humidity observations. Overall, the OBSCTH and
698 OBSBT predictors were the most useful because not only did their use lead to more accurate cloud
699 and water vapor fields in the prior analyses, but they also produced the smallest RMSEs for the
700 wind and temperature fields.

701 *c. Symmetric Bias Correction Predictors*

702 In this section, we assess the impact of using "symmetric" predictors to remove the bias from all-
703 sky infrared brightness temperatures. As discussed in the introduction, symmetric predictors that
704 represent the average of an observed quantity and its corresponding model equivalent have been
705 extensively used when developing all-sky observation error models. First introduced by Geer and

706 Bauer (2011), symmetric predictors have been shown in various studies to lead to more Gaussian
707 OMB departure statistics when a suitable cloud impact parameter is used to dynamically assign
708 the error variance to each observation. This symmetric observation error approach is now widely
709 used by operational DA systems that assimilate all-sky microwave radiances because it leads to
710 more accurate forecasts through better utilization of the satellite observations.

711 Despite their widespread application in all-sky observation error models, it is not clear if sym-
712 metric variables are effective bias predictors, especially in the presence of complex nonlinear bias
713 patterns. To explore their potential utility, two additional sets of experiments were run where the
714 cloud top height or the $6.2 \mu\text{m}$ brightness temperatures were used as the bias predictor. These vari-
715 ables were chosen because they are either a direct measure of, or are sensitive to, the cloud height,
716 which is an excellent measure of cloud impact in all-sky infrared brightness temperatures. Experi-
717 ments were performed where observed (BC-OBSBT, BC-OBSCTH), simulated (BC-SIMBT, BC-
718 SIMCTH), or symmetric (BC-SYMBT, BC-SYMCTH) quantities for each BC predictor variable
719 were used to remove the bias from the infrared brightness temperatures prior to their assimilation.
720 For the simulated cloud top height predictor, the cloud top was identified as the first model level
721 looking downward from the model top in which the vertically-integrated cloud hydrometeor mix-
722 ing ratio was $> 10^{-4} \text{ kg kg}^{-1}$. All of the cloud hydrometeor species predicted by the microphysics
723 parameterization scheme were used when computing this quantity. The modeled land/ocean sur-
724 face elevation was used as the predictor value when the accumulated cloud mixing ratio threshold
725 was not surpassed. The same approach was used for the observed cloud top height retrievals where
726 grid points identified as clear were also set to the model surface elevation.

727 Summary statistics showing the percentage changes relative to the No-BC experiment for the
728 radiosonde temperature, relative humidity, and zonal and meridional wind speed observations are
729 shown in Tables 4 and 5, respectively, for experiments using the various $6.2 \mu\text{m}$ brightness tem-

730 perature or cloud top height quantities as the bias predictor. These statistics were computed using
731 output from the prior ensemble mean analyses. Overall, the results show that using symmetric bias
732 predictors does not lead to a more accurate model background. For experiments using the $6.2 \mu\text{m}$
733 brightness temperature predictors (Table 4), the error reduction for each radiosonde observation
734 type is smaller during the BC-SYMBT experiment than it is during the BC-OBSBT experiment.
735 Likewise, when the cloud top height quantities are used as the bias predictors (Table 5), the most
736 accurate analyses are obtained when the observed quantity is used during the BC-OBSCTH ex-
737 periment. The error reductions during the BC-SYMCTH experiment are either in between those
738 obtained during the BC-OBSCTH and BC-SIMCTH experiments, or are smaller than both of them.
739 A possible reason for the relatively poor performance during both of the symmetric bias predictor
740 experiments is that, with the exception of relative humidity, the error reductions are consistently
741 smaller when the simulated predictors are used to remove the bias from the all-sky infrared obser-
742 vations. Thus, inclusion of the model-simulated predictor value when computing the symmetric
743 bias predictor is not beneficial. Instead, it is more effective to simply use the observed quantity as
744 the bias predictor.

745 To examine this behavior more closely, Fig. 11 shows 2-D probability distributions for the en-
746 semble mean $6.2 \mu\text{m}$ brightness temperature BCs and innovations when the simulated, observed,
747 and symmetric cloud top height bias predictors are used. Similar results are obtained for experi-
748 ments employing the $6.2 \mu\text{m}$ brightness temperature predictors (not shown). Comparison of the
749 BC distributions reveals a relatively flat pattern during the BC-SIMCTH experiment (Fig. 11a),
750 which shows that the model-simulated version of the cloud top height predictor is unable to ac-
751 count for the large negative conditional biases for brightness temperatures $< 230 \text{ K}$ (Fig. 2a). The
752 smaller BCs for the lower brightness temperatures during this experiment stands in sharp contrast
753 to the much larger BCs during the BC-OBSCTH experiment (Fig. 11e). Because the symmetric

754 predictor is simply the mean of the observed and simulated quantities, the BC distribution during
755 the BC-SYMCTH experiment (Fig. 11c) is a hybrid of the BC-OBSCTH and BC-SIMCTH dis-
756 tributions. As such, the smaller BCs for the lower brightness temperatures due to the impact of
757 the model-simulated quantity leads to larger innovations than occurred during the BC-OBSCTH
758 experiment (Fig 11d, f). As was shown in the previous section, experiments containing larger in-
759 novations for the lower brightness temperatures associated with optically thick upper-level clouds
760 were generally less accurate when assessed using radiosonde observations. This result suggests
761 that, though symmetric predictors have been shown to improve the performance of all-sky obser-
762 vation error models, they may not work as well for all-sky BC. Further studies using other satellite
763 bands and models are necessary to explore this in more detail.

764 **4. Discussion and Conclusions**

765 In this study, ensemble DA experiments were performed using the regional-scale KENDA sys-
766 tem to evaluate the ability of all-sky infrared brightness temperatures to improve the accuracy of
767 the ensemble prior analyses used during each assimilation cycle. Observations from the $6.2 \mu\text{m}$
768 band on the SEVIRI sensor were assimilated at hourly intervals over a 3-day period in May 2014.
769 This infrared band is primarily sensitive to clouds and water vapor in the upper troposphere. Var-
770 ious experiments were performed in which different BC predictors were used to remove biases
771 from the all-sky brightness temperatures prior to their assimilation. Results from these BC exper-
772 iments were compared to baseline experiments in which the brightness temperature were either
773 not assimilated (No-BC) or were assimilated without first removing their biases (No-BC). This
774 study builds upon the passive monitoring experiments described in Otkin et al. (2018) by explor-
775 ing the impact of linear and nonlinear BC predictors during experiments in which all-sky infrared
776 brightness temperatures are actively assimilated.

777 Overall, inspection of the $6.2 \mu\text{m}$ brightness temperature OMB departure distribution from the
778 No-Assim experiment revealed that the conditional biases exhibited a nonlinear pattern character-
779 ized by small biases for higher brightness temperatures and increasingly large negative biases for
780 lower brightness temperatures. Though the negative conditional biases are likely at least partially
781 due to inaccuracies in the forward observation operator, they also indicate that the model analyses
782 do not contain enough cloud condensate in the upper troposphere. This deficiency, whether due to
783 insufficient spatial coverage or cloud optical depth, represents a systematic bias in the NWP model
784 depiction of the cloud field. Thus, trying to add these upper-level clouds during an assimilation
785 cycle could be problematic because of aliasing of the cloud information onto other model state
786 variables and the tendency for the model to revert back to its preferred state during the subsequent
787 forecast period.

788 Evaluation of the No-BC experiment showed that assimilation of the infrared brightness tem-
789 peratures without first removing their biases almost always degraded the accuracy of the ensemble
790 prior analyses based on larger OMB departures for the radiosonde observations. In particular, the
791 summary statistics showed that the relative humidity bias and RMSE were much larger during this
792 experiment than they were during the No-Assim experiment. Despite having strong sensitivity to
793 water vapor in the upper troposphere, assimilating infrared brightness temperatures without BC
794 actually increased the relative humidity RMSE, primarily because of a large increase in the moist
795 bias already present in the No-Assim experiment. The No-BC experiment was also characterized
796 by smaller $6.2 \mu\text{m}$ brightness temperature OMB departures, which suggests that instead of adding
797 clouds to the analysis that the DA system instead added more water vapor. An alternative expla-
798 nation is that a portion of the cloud condensate added to the ensemble posterior analyses during
799 a given assimilation cycle evaporated during the subsequent model integration period, thereby in-
800 creasing the moist bias. Regardless, this result suggests that the analyses were being too strongly

801 constrained by the all-sky infrared brightness temperatures during the No-BC experiment in situ-
802 ations where the model was unable to properly handle the additional cloud information.

803 The subsequent removal of linear and nonlinear conditional biases from the all-sky brightness
804 temperatures through use of a 3rd order polynomial expansion of the OMB departures and various
805 BC predictors led to smaller errors for all of the radiosonde observation types when compared to
806 the No-BC experiment. The largest improvements occurred for the relative humidity observations
807 where the moist bias in the upper troposphere was greatly reduced. Notable improvements also
808 occurred in the temperature bias and in the RMSE for the zonal and meridional wind speed com-
809 ponents during the BC-OBSBT and BC-OBSCTH experiments. The temperature RMSE was also
810 smaller in most of the troposphere; however, a spike of larger errors near and above the tropopause
811 led to a neutral impact when all temperature observations were considered.

812 Comparison of the various predictors showed that those sensitive to the location of the cloud top
813 had the largest positive impact on the model background based on improved fits to the radiosonde
814 observations. The observed cloud top height and observed $6.2 \mu\text{m}$ brightness temperature predic-
815 tors were the best overall because their use not only led to the smallest relative humidity errors, but
816 also led to the largest error reductions for the zonal and meridional wind speed observations and
817 the smallest degradation for the temperature RMSE. Both of these predictors also improved the
818 cloud field much more than the other predictors, as signified by the smaller brightness temperature
819 RMSE and bias. The larger improvements during the BC-OBSBT and BC-OBSCTH experiments
820 were primarily due to the ability of the cloud-sensitive predictors to more effectively remove the
821 large negative biases from brightness temperatures $< 230 \text{ K}$. The larger BCs for these clouds
822 then led to smaller brightness temperature innovations and presumably fewer model spin-up prob-
823 lems during the subsequent 1-h forecasts. Additional experiments using the OBSCTH predictor
824 revealed that it was beneficial to use higher order nonlinear BC terms to remove the bias from

825 the all-sky infrared brightness temperatures. For example, the radiosonde OMB departure errors
826 generally decreased as the order of the polynomial expansion increased from the 0th order to the
827 3rd order. Finally, an additional set of experiments showed that symmetric bias predictors do not
828 improve the model analyses as effectively as the observed predictors do by themselves. This sug-
829 gests that, though symmetric predictors have proven utility for all-sky observation error models,
830 they may not be as useful when developing all-sky BC methods.

831 This study has shown that assimilation of all-sky infrared brightness temperatures substantially
832 improves the accuracy of the cloud and water vapor fields in the prior ensemble analyses when
833 cloud-sensitive predictors and higher order BC terms are used to remove linear and nonlinear con-
834 ditional biases from the observations prior to their assimilation. Though encouraging, additional
835 studies are necessary to evaluate the ability of the NBC method and the all-sky infrared bright-
836 ness temperatures to improve the model analyses during other seasons containing different cloud
837 regimes potentially characterized by different conditional bias patterns. It will also be necessary to
838 perform ensemble forecasts to evaluate how long the improved cloud and water vapor fields per-
839 sist during the forecast period. It is important to note that the experiments performed during this
840 study are only an initial step toward inclusion of the all-sky infrared observations in the KENDA
841 system and that additional developments have the potential to substantially increase their impact.
842 For example, there is great promise in pairing the BC method to a dynamic all-sky observation
843 error model because that could lead to more effective use of the clear- and cloudy-sky brightness
844 temperatures. It would also be helpful to explore the benefits of more frequent assimilation up-
845 dates and in assimilating brightness temperatures from more than one infrared band, though that
846 would require development of a correlated observation error model. The results also suggested
847 that attention should be given to developing methods that can increase the ensemble spread in the
848 cloud hydrometeor variables. These topics are all left to future work.

849 *Acknowledgments.* We gratefully acknowledge Jesse Stroik from the University of Wisconsin-
850 Madison and Hendrik Reich, Andreas Rhodin, Robin Faulwetter, and Axel Hutt from the German
851 DWD for their assistance porting and installing the KENDA system and basic cycling (BACY)
852 scripts to the NOAA/NESDIS/STAR "S4" supercomputer located at the University of Wisconsin-
853 Madison. The S4 supercomputer (Boukabara et al. 2016) was used to perform all of the cycled
854 DA experiments. The lead author was partially supported by a University of Reading International
855 Research Studentship.

856 **5. References**

857 Aksoy, A., D. C. Dowell, and C. Snyder, 2009: A multicas e comparative assessment of the
858 ensemble Kalman filter for assimilation of radar observations. Part I: Storm-scale analysis. *Mon.*
859 *Wea. Rev.*, 137, 1805–1824.

860 Aonashi, K. and H. Eito, 2011: Displaced ensemble variations assimilation method to incor-
861 porate microwave imager brightness temperatures into a cloud resolving model. *Journal of the*
862 *Meteorological Society of Japan*, 89, 175–194, 2011 175 DOI:10.2151/jmsj.2011-301.

863 Anderson J., and S. Anderson, 1999: A Monte Carlo implementation of the nonlinear filtering
864 problem to produce ensemble assimilations and forecasts. *Mon. Wea. Rev.*, 127, 2741-2758.

865 Aravequia J.A., I. Szunyogh, E. J. Fertig, E. Kalnay, D. Kuhl, and E. J. Kostelich, 2011: Eval-
866 uation of a strategy for the assimilation of satellite radiance observations with the local ensemble
867 transform Kalman filter. *Mon. Weather Rev.*, 139, 1932-1951, doi: 10.1175/2010MWR3515.1.

868 Auligne T., A. P. McNally, and D. P. Dee, 2007: Adaptive bias correction for satellite data in a
869 numerical weather prediction system. *Q. J. R. Meteorol. Soc.*, 133, 631-642.

870 Baldauf M., A. Seifert, J. Forstner, D. Majewski, M. Raschendorfer, and T. Reinhardt, 2011:
871 Operational convective-scale numerical weather prediction with the COSMO Model: Description
872 and sensitivities. *Mon. Weather Rev.*, 139, 3887–3905.

873 Baordo F., and A. J. Geer, 2016: Assimilation of SSMIS humidity-sounding channels in all-sky
874 conditions over land using a dynamic emissivity retrieval. *Q. J. R. Meteorol. Soc.* 142, 2854–2866,
875 <https://doi.org/10.1002/qj.2873>.

876 Bauer P., A. J. Geer, P. Lopez, and D. Salmond, 2010: Direct 4D-Var assimilation of all-sky
877 radiances: Part I. Implementation. *Q. J. R. Meteorol. Soc.*, 136, 1868–1885.

878 Bauer P., and Coauthors, 2011: Satellite cloud and precipitation assimilation at operational NWP
879 centres. *Q. J. R. Meteorol. Soc.*, 137, 1934–1951.

880 Baum, B. A., P. Yang, A. J. Heymsfield, A. Bansemer, A. Merrelli, C. Schmitt, and C.
881 Wang, 2014: Ice cloud bulk single-scattering property models with the full phase matrix at
882 wavelengths from 0.2 to 100 μm . *J. Quant. Spectrosc. Radiat. Transfer*, 146, 123–139,
883 [doi:10.1016/j.jqsrt.2014.02.029](https://doi.org/10.1016/j.jqsrt.2014.02.029).

884 Bengtsson L., and K. Hodges, 2005: On the impact of humidity observations in numerical
885 weather prediction. *Tellus*, 57A, 701–708.

886 Berner, J., and Coauthors, 2017: Stochastic parameterization: Toward a new view of weather
887 and climate models. *Bull. Amer. Meteor. Soc.*, 98, 565–588.

888 Bessho, K., and Coauthors, 2016: An introduction to Himawari-8/9—Japan’s new-
889 generation geostationary meteorological satellites. *J. Meteor. Soc. Japan*, 94, 151–183,
890 [doi:https://doi.org/10.2151/jmsj.2016-009](https://doi.org/10.2151/jmsj.2016-009).

891 Bocquet M., C. A. Pires, and L. Wu, 2010: Beyond Gaussian statistical modelling in geophysical
892 data assimilation. *Mon. Wea. Rev.*, 138, 2997–3023.

893 Bormann N., A. J. Geer, and P. Bauer, 2011: Estimates of observation-error characteristics in
894 clear and cloudy regions for microwave imager radiances from NWP. *Q. J. R. Meteorol. Soc.*, 137,
895 2014–2023.

896 Bormann, N., M. Bonavita, R. Dragani, R. Eresmaa, M. Matricardi, and A. McNally, 2016: En-
897 hancing the impact of IASI observations through an updated observation-error covariance matrix.
898 *Q. J. R. Meteorol. Soc.*, 142, 1767–178, <https://doi.org/10.1002/qj.2774>.

899 Boukabara, S. A., and Coauthors, 2016: S4: An O2R/R2O infrastructure for optimizing satel-
900 lite data utilization in NOAA numerical modeling systems, a significant step toward bridging the
901 valley of death. *Bull. Am. Meteorol. Soc.*, 97, 2379-2394.

902 Campbell, W. F., E. A. Satterfield, B. Ruston, and N. L. Baker, 2017: Accounting for correlated
903 observation error in a dual-formulation 4D variational data assimilation system. *Mon. Wea. Rev.*,
904 145, 1019–1032, <https://doi.org/>.

905 Cintineo, R., Otkin, J.A., Xue, M., Kong, F., 2014. Evaluating the performance of planetary
906 boundary layer and cloud microphysical parameterization schemes in convection permitting en-
907 semble forecasts using synthetic GOES-13 satellite observations. *Mon. Wea. Rev.* 142, 163-182.

908 Cintineo, R., J. A. Otkin, T. Jones, S. Koch, and D. J. Stensrud, 2016: Assimilation of syn-
909 thetic GOES-R ABI infrared brightness temperatures and WSR-88D radar observations in a high-
910 resolution OSSE. *Mon. Wea. Rev.*, 144, 3159-3180.

911 Dee, D. P., 2005: Bias and data assimilation. *Q. J. R. Meteorol. Soc.*, 131, 3323-3343, doi:
912 10.1256/qj.05.137.

913 Dee D. P., and S. Uppala, 2009: Variational bias correction of satellite radiance data in the
914 ERA-Interim reanalysis. *Q. J. R. Meteorol. Soc.* 135: 1830-1841.

915 Derber J. C., D. F. Parrish, and S. J. Lord, 1991: The new global operational analysis system at
916 the National Meteorological Center. *Weather and Forecasting*, 6, 538-547.

917 Derber, J. C., and W.-S. Wu, 1998: The use of TOVS cloud-cleared radiances in the NCEP SSI
918 analysis system, *Mon. Weather Rev.*, 126, 2287-2299.

919 Derrien M., and H. Le Gleau, 2005: MSG/SEVIRI cloud mask and type from SAF NWC. *Int.*
920 *J. Remote Sens.*, 26, 4707-4732.

921 Dowell, D. C., F. Zhang, L. Wicker, C. Snyder, and N. A. Crook, 2004: Wind and temperature
922 retrievals in the 17 May 1981 Arcadia Oklahoma, supercell: Ensemble Kalman filter experiments.
923 *Mon. Wea. Rev.*, 132, 1982–2005.

924 Eikenberg, S., C. Kohler, A. Siefert, and S. Crewell, 2015: How microphysical choices affect
925 simulated infrared brightness temperatures. *Atmos. Research*, 156, 67-79.

926 Errico R. M., P. Bauer, and J.-F. Mahfouf, 2007: Issues regarding the assimilation of cloud and
927 precipitation data. *J. Atmos. Sci.*, 64, 3785–3798.

928 Eyre J. R., 1992: A bias correction scheme for simulated TOVS brightness temperatures. Tech-
929 nical Memorandum 176, Reading, UK:,ECMWF.

930 Eyre, J. R., 2016: Observation bias correction schemes in data assimilation systems: a theoret-
931 ical study of some of their properties. *J. Q. R. Meteorol. Soc.*, 142, 2284-2291.

932 Fabry, F., and J. Sun, 2010: For how long should what data be assimilated for the mesoscale
933 forecasting of convection and why? Part I: On the prop-agation of initial condition errors and
934 their implications for data assimila- tion, *Mon. Wea. Rev.*, 138, 242–255.

935 Fertig E.J., S.-J. Baek, B. R. Hunt, E. Ott, I. Szunyogh, J. A. Aravequia, E. Kalnay, H. Li, and
936 J. Liu, 2009: Observation bias correction with an ensemble Kalman filter. *Tellus*, 61A, 210-226,
937 doi: 10.1111/j.1600-0870.2008.00378.x.

938 Geer A. J., and P. Bauer, 2011: Observation errors in all-sky data assimilation. *Q. J. R. Meteorol.*
939 *Soc.*, 137, 2024–2037.

940 Geer A. J., P. Bauer, and S. J. English, 2012: ‘Assimilating AMSU-A temperature sounding
941 channels in the presence of cloud and precipitation’. Technical Memorandum 670, European
942 Centre for Medium-range Weather Forecasts (ECMWF), Reading, UK.

943 Geer A. J., F. Baordo, N. Bormann, and S. English, 2014: All-sky assimilation of microwave
944 humidity sounders. Technical Memorandum 741, European Centre for Medium-range Weather
945 Forecasts (ECMWF), Reading, UK.

946 Geer, A. J., and Coauthors, 2017: The growing impact of satellite observations sensitive
947 to humidity, cloud and precipitation, *Quart. J. Roy. Meteorol. Soc.*, 143, 3189–3206,
948 <https://doi.org/10.1002/qj.3172>.

949 Geer, A. J., and Coauthors, 2018: All-sky satellite data assimilation at operational weather fore-
950 casting centres, *Quart. J. Roy. Meteorol. Soc.*, 144, 1191–1217, <https://doi.org/10.1002/qj.3202>.

951 Geer, A. J., S. Migliorini, and M. Matricardi, 2019: All-sky assimilation of infrared radiances
952 sensitive to mid- and upper-tropospheric moisture and cloud. *Atmos. Meas. Tech.*, under review.

953 Le Gleau H., 2016: Algorithm theoretical basis document for the cloud products processors of
954 the NWC/GEO. <http://www.nwcsaf.org> (accessed 29 March 2017).

955 Guidard V., N. Fourrie, P. Brousseau, and F. Rabier, 2011: Impact of IASI assimilation at global
956 and convective scales and challenges for the assimilation of cloudy scenes. *Q. J. R. Meteorol.*
957 *Soc.*, 137, 1975–1987.

958 Gustafsson, N., and Coauthors, 2018: Survey of data assimilation methods for convective-scale
959 numerical weather prediction at operational centres. *Q. J. R. Meteorol. Soc.*, 144, 1218-1256,
960 <https://doi.org/10.1002/qj.3179>.

961 Harnisch F., M. Weissmann, and A. Perianez, 2016: Error model for the assimilation of cloud-
962 affected infrared satellite observations in an ensemble data assimilation system. *Q. J. R. Meteorol.*
963 *Soc.*, 142, 1797–1808.

964 Harris, B. A, and G. Kelly, 2001: A satellite radiance-bias correction scheme for data assimila-
965 tion. *Q. J. R. Meteorol. Soc.*, 127, 1453-1468.

966 Heillette, S., and L. Garand, 2007: A practical approach for the assimilation of cloudy infrared
967 radiances and its evaluation using AIRS simulated observations, *Atmos. Ocean*, 45, 211–225.

968 Hilton F., N. C. Atkinson, S. J. English, and J. R. Eyre, 2009: Assimilation of IASI at the Met
969 Office and assessment of its impact through observing system experiments. *Q. J. R. Meteorol.*
970 *Soc.*, 135, 495-505.

971 Hocking J., P. Rayer, R. Saunders, M. Matricardi, A. Geer, P. Brunet, 2011: RTTOV v10 Users
972 Guide, NWC SAF report. EUMETSAT: Darmstadt, Germany.

973 Honda, T., and Coauthors, 2018a: Assimilating all-sky Himawari-8 satellite infrared ra-
974 diances: A case of Typhoon Soudelor (2015). *Mon. Wea. Rev.*, 146, 213–229,
975 <https://doi.org/10.1175/MWR-D-16-0357.1>.

976 Honda, T., S. Kotsuki, G.-Y. Lien, Y. Maejima, K. Okamoto, and Y. Miyoshi, 2018b: Assimila-
977 tion of Himawari-8 All-Sky Radiances Every 10Minutes: Impact on Precipitation and Flood Risk
978 Prediction. *J. Geophys. Res.*, 123, 965-976, 10.1002/2017JD027096.

979 Houtekamer, P. L., and F. Zhang, 2016: Review of the ensemble Kalman filter for atmospheric
980 data assimilation. *Mon. Wea. Rev.*, 144, 4489-4532.

981 Hunt B. R., E. J. Kostelich, and I. Szunyogh, 2007: Efficient data assimilation for spa-
982 tiotemporal chaos: A local ensemble transform Kalman filter. *Physica D*, 230, 112-126,
983 [doi:10.1016/j.physd.2006.11.008](https://doi.org/10.1016/j.physd.2006.11.008).

984 Jones, T. A., J. A. Otkin, D. J. Stensrud, and K. Knopfmeier, 2013a: Assimilation of satellite in-
985 frared radiances and Doppler radar observations during a cool season observing system simulation
986 experiment. *Mon. Wea. Rev.*, 141, 3273–3299, [doi:10.1175/MWR-D-12-00267.1](https://doi.org/10.1175/MWR-D-12-00267.1).

987 Jones, T. A., D. J. Stensrud, P. Minnis, and R. Palikonda, 2013b: Evaluation of a forward
988 operator to assimilate cloud water path into WRF-DART. *Mon. Wea. Rev.*, 141, 2272–2289,
989 doi:10.1175/MWR-D-12-00238.1.

990 Jones, T. A., J. A. Otkin, D. J. Stensrud, and K. Knopfmeier, 2014: Forecast evaluation of an
991 Observing System Simulation Experiment assimilating both radar and satellite data. *Mon. Wea.*
992 *Rev.*, 142, 107–124, doi:10.1175/MWR-D-13-00151.1.

993 Jones, T. A., and D. J. Stensrud, 2015: Assimilating cloud water path as a function of
994 model cloud microphysics in an idealized simulation. *Mon. Wea. Rev.*, 143, 2052–2081,
995 doi:10.1175/MWR-D-14-00266.1.

996 Jones, T. A., D. J. Stensrud, L. Wicker, P. Minnis, and R. Palikonda, 2015: Simultaneous radar
997 and satellite data storm-scale assimilation using an ensemble Kalman filter approach for 24 May
998 2011. *Mon. Wea. Rev.*, 143, 165–194, doi:10.1175/MWR-D-14-00180.1.

999 Jones, T. A., K. Knopfmeier, D. Wheatley, G. Creager, P. Minnis, and R. Palikondo, 2016: The
1000 NSSL Multiscale Ensemble. Part II: Combined radar and satellite assimilation. *Wea. Forecasting*,
1001 31, 297–327, doi:10.1175/WAF-D-15-0107.1.

1002 Jones, T. A., X. G. Wang, P. Skinner, A. Johnson, and Y. M. Wang, 2018: Assimilation of
1003 GOES-13 Imager Clear-Sky Water Vapor (6.5 μm) Radiances into a Warn-on-Forecast System.
1004 *Mon. Wea. Rev.*, 146, 1077–1107, doi:10.1175/MWR-D-17-0280.1.

1005 Kazumori, M., A. J. Geer, and S. J. English, 2016: Effects of all-sky assimilation of GCOM-
1006 W/AMS2 radiances in the ECMWF numerical weather prediction system, *Q. J. R. Meteorol.*
1007 *Soc.*, 142, 721–737, <https://doi.org/10.1002/qj.2669>.

1008 Kerr, C. A., D. J. Stensrud, and X. Wang, 2015: Assimilation of cloud-top temperature and radar
1009 observations of an idealized splitting supercell using an observing system simulation experiment.
1010 *Mon. Wea. Rev.*, 143, 1018–1034, <https://doi.org/10.1175/MWR-D-14-00146.1>.

1011 Klaes, K. D., and Coauthors, 2007: An introduction to the EUMET- SAT Polar System, Bull.
1012 Amer. Meteor. Soc., 88, 1085–1096.

1013 Kostka P. M., M. Weissmann, R. Buras, B. Mayer, and O. Stiller, 2014: Observation operator
1014 for visible and near-infrared satellite reflectances. *J. Atmos. Oceanic Technol.*, 31, 1216-1233.

1015 Kurzrock, F., S. Cros, F. Chane-Ming, J. A. Otkin, L. Linguet, A. Hutt, G. Lajoie, and R.
1016 Potthast, 2018: The assimilation of geostationary meteorological satellite observations in regional
1017 NWP for cloudiness forecasting. *Meteorologische Zeitschrift*, 27, 277-298.

1018 Langland, R. H. and N. L. Baker, 2004: Estimation of observation impact using the NRL atmo-
1019 spheric variational data assimilation adjoint system. *Tellus A.*, 56, 189-201.

1020 Lawrence, H., N. Bormann, A. J. Geer, Q. Lu, and S. J. English, 2018: Evaluation and
1021 Assimilation of the Microwave Sounder MWHS-2 Onboard FY-3C in the ECMWF Numerical
1022 Weather Prediction System, *IEEE Transactions on Geoscience and Remote Sensing*, 56, 3333-
1023 3349, DOI:10.1109/TGRS.2018.2798292.

1024 Lien, G.-Y., T. Miyoshi, and E. Kalnay, 2016: Assimilation of TRMM Multisatellite Precipi-
1025 tation Analysis with a Low-Resolution NCEP Global Forecast System, *Mon. Wea. Rev.*, 144,
1026 643–661.

1027 Lin, H., S. Weygandt, S. Benjamin, and M. Hu, 2017: Satellite radiance data assimilation with
1028 the hourly updated rapid refresh. *Wea. Forecasting*, 32, 1273–1287, [https://doi.org/10.1175/WAF-](https://doi.org/10.1175/WAF-D-16-0215.1)
1029 [D-16-0215.1](https://doi.org/10.1175/WAF-D-16-0215.1).

1030 Lin Y. L., R. Farley, and H. Orville, 1983: Bulk parameterization of the snow field in a cloud
1031 model. *J. Climate Appl. Meteor.*, 22, 1065-1092.

1032 Lupu C., and A. P. McNally, 2012: Assimilation of cloud-affected radiances from Meteosat-9
1033 at ECMWF. EUMETSAT/ECMWF Fellowship Programme Research Report No. 25. ECMWF,
1034 Reading, UK.

1035 Mahfouf, J.-F., 2010: Assimilation of satellite-derived soil moisture from ASCAT in a limited-
1036 area NWP model. *Q. J. R. Meteorol. Soc.*, 136, 784-798, DOI:10.1002/qj.602.

1037 Majewski, D. and coauthors, 2002: The Operational Global Icosahedral-Hexagonal Gridpoint
1038 Model GME: Description and High-Resolution Tests. *Mon. Wea. Rev.*, 130, 319-338.

1039 Matricardi M., 2005: The inclusion of aerosols and clouds in RTIASI, the ECMWF Fast Radia-
1040 tive Transfer Model for the Infrared Atmospheric Sounding Interferometer, Technical Memorandum
1041 474, ECMWF, Reading, UK.

1042 McFarquhar, G. M., S. Iacobellis, and R. C. J., Somerville, 2003: SCM simulations of tropical
1043 ice clouds using observationally based parameterizations of microphysics. *J. Clim.*, 16, 1643-
1044 1664.

1045 McNally A. P., 2002: A note on the occurrence of cloud in meteorologically sensitive areas and
1046 the implications for advanced infrared sounders. *Q. J. R. Meteorol. Soc.*, 128, 2551-2556.

1047 McNally, A. P., 2009: The direct assimilation of cloud-affected satellite infrared radiances in the
1048 ECMWF 4D-Var. *Q. J. R. Meteorol. Soc.*, 135, 1214-1229.

1049 Minamide, M., and F. Zhang, 2017: Adaptive observation error inflation for assimilating all-sky
1050 satellite radiance. *Mon. Wea. Rev.*, 145, 1063-1081, <https://doi.org/10.1175/MWR-D-16-0257.1>.

1051 Minamide, M., and F. Zhang, 2018: Assimilation of all-sky infrared radiances from Himawari-8
1052 and impacts of moisture and hydrometer initialization on convection-permitting tropical cyclone
1053 prediction. *Mon. Wea. Rev.*, 146, 3241-3258.

1054 Miyoshi T., Y. Sato, and T. Kadowaki, 2010: Ensemble Kalman filter and 4D-Var intercompar-
1055 ison with the Japanese operational global analysis and prediction system. *Mon. Wea. Rev.*, 138,
1056 2846-2866, doi:10.1175/2010MWR3209.1.

1057 Nakamura, G., and R. Potthast, 2015: Inverse Modeling: An Introduction to the Theory and
1058 Methods of Inverse Problems and Data Assimilation. IOP Publishing, 312 pp., doi:10.1088/978-
1059 0-7503-1218-9.

1060 Okamoto K., 2013: Assimilation of overcast cloudy infrared radiances of the geostationary
1061 MTSAT-1R imager. *Q. J. R. Meteorol. Soc.*, 139, 715–730.

1062 Okamoto K., A. P. McNally, and W. Bell, 2014: Progress towards the assimilation of all-sky
1063 infrared radiances: An evaluation of cloud effects. *Q. J. R. Meteorol. Soc.*, 140, 1603–1614.

1064 Otkin, J. A., and T. J. Greenwald, 2008: Comparison of WRF model-simulated and MODIS-
1065 derived cloud data. *Mon. Wea. Rev.*, 136, 1957-1970.

1066 Otkin, J. A., 2010: Clear and cloudy sky infrared brightness temperature assimilation using an
1067 ensemble Kalman filter. *J. Geophys. Res.*, 115, D19207, doi:10.1029/2009JD013759.

1068 Otkin, J. A., 2012a: Assessing the impact of the covariance localization radius when assimilating
1069 infrared brightness temperature observations using an ensemble Kalman filter. *Mon. Wea. Rev.*,
1070 140, 543–561, doi:10.1175/MWR-D-11-00084.1.

1071 Otkin, J. A., 2012b: Assimilation of water vapor sensitive infrared brightness tempera-
1072 ture observations during a high impact weather event. *J. Geophys. Res.*, 117, D19203,
1073 doi:10.1029/2012JD017568.

1074 Otkin, J. A., R. Potthast, and A. Lawless, 2018: Nonlinear bias correction for satellite data
1075 assimilation using Taylor series polynomials. *Mon. Wea. Rev.*, 146, 263-285.

1076 Pan, S. J., J. D. Gao, D. J. Stensrud, X. G. Wang, and T. A. Jones, 2018: Assimilation of
1077 Radar Radial Velocity and Reflectivity, Satellite Cloud Water Path, and Total Precipitable Water
1078 for Convective-Scale NWP in OSSEs. *J. Atmos. Oceanic Technol.*, 35, 67-89

1079 Pangaud, T., N. Fourrie, V. Guidard, M. Dahoui, F. and Fabier, 2009: Assimilation of
1080 AIRS radiances affected by mid to low level clouds. *Mon. Wea. Rev.*, 137, 4276–4292.
1081 <https://doi.org/10.1175/2009MWR3020.1>.

1082 Perianez A., H. Reich, and R. Potthast, 2014: Optimal localization for ensemble Kalman filter
1083 systems. *J. Meteorol. Soc. Jpn.* 92: 585–597. <https://doi.org/10.2151/jmsj.2014-605>.

1084 Pavelin, E.G., S. J. English, and J. R. Eyre, 2008: The assimilation of cloud-affected infrared
1085 satellite radiances for numerical weather prediction. *Q. J. R. Meteorol. Soc.*, 13, 737–749.

1086 Parrish D. F., and J. C. Derber, 1992: The National Meteorological Center’s spectral statistical
1087 interpolation analysis system. *Mon. Wea. Rev.*, 120, 1747-1763.

1088 Peubey, C. and A. P. McNally, 2009: Characterization of the impact of geostationary clear-sky
1089 radiances on wind analyses in a 4D-Var context, *Q. J. R. Meteorol. Soc.*, 135, 1863–1876.

1090 Raisanen, P., 1998: Effective longwave cloud fraction and maximum-random overlap of clouds:
1091 A problem and a solution. *Mon. Wea. Rev.*, 126, 3336?3340.

1092 Raschendorfer M., 2001: The new turbulence parameterisation of LM. *COSMO Newsl.* 1, 89-
1093 97.

1094 Ritter B., and J. F. Geleyn, 1992: A comprehensive radiation scheme for numerical weather
1095 prediction models with potential applications in climate simulations. *Mon. Wea. Rev.* 120, 303-
1096 325

1097 Saunders R., M. Matricardi, and P. Brunel, 1999: An improved fast radiative transfer model for
1098 assimilation of satellite radiance observations. *Q. J. R. Meteorol. Soc.*, 125, 1407-1425.

1099 Schmit, T. J., P. Griffith, M. M. Gunshor, J. M. Daniels, S. J. Goodman, and W. J. Lebar,
1100 2017: A closer look at the ABI on the GOES-R series. *Bull. Amer. Meteor. Soc.*, 98, 681–698,
1101 <https://doi.org/10.1175/BAMS-D-15-00230.1>.

1102 Schomburg A., C. Schraff, and R. Potthast, 2015: A concept for the assimilation of satellite
1103 cloud information in an Ensemble Kalman Filter: Single-observation experiments. *Q. J. R. Mete-*
1104 *orol. Soc.* 141: 893–908, doi: 10.1002/qj.2407.

1105 Schraff, C., H. Reich, A. Rhodin, A. Schomburg, K. Stephan, A. Perianez, and R. Potthast, 2016:
1106 Kilometer-Scale ensemble data assimilation for the COSMO model (KENDA). *Q. J. R. Meteorol.*
1107 *Soc.*, 142, 1453-1472.

1108 Schmetz, J., P. Pili, S. Tjemkes, D. Just, J. Lerkmann, S. Rota, and A. Ratier, 2002: An intro-
1109 duction to Meteosat Second Generation (MSG). *Bull. Amer. Meteor. Soc.*, 83, 977-992.

1110 Seifert A, and K. Beheng, 2001: A double-moment parameterization for simulating auto-
1111 conversion, accretion and selfcollection. *Atmos. Res.*, 59-60, 265-281, doi:10.1016/S0169-
1112 8095(01)00126-0.

1113 Stengel, M., P. Uden, M. Lindskog, P. Dahlgren, N. Gustafsson, and R. Bennartz, 2009: As-
1114 simulation of SEVIRI infrared radiances with HIRLAM 4D-Var. *Quart. J. Roy. Meteor. Soc.*, 135,
1115 2100–2109, doi:10.1002/qj.501.

1116 Stengel, M., M. Lindskog, P. Uden, and N. Gustafsson, 2013: The impact of cloud-affected IR
1117 radiances on forecast accuracy of a limited- area NWP model. *Quart. J. Roy. Meteor. Soc.*, 139,
1118 2081–2096, doi:10.1002/qj.2102.

1119 Strow, L. L., and Coauthors, 2013: Spectral calibration and valida- tion of the Cross-track In-
1120 frared Sounder on the Suomi NPP satellite. *J. Geophys. Res. Atmos.*, 118, 12 486– 12 496,
1121 <https://doi.org/10.1002/2013JD020480>.

1122 Szunyogh, I., E. J. Kostelich, G. Gyarmati, E. Kalnay, and B. R Hunt, 2008: A local ensemble
1123 transform Kalman filter data assimilation system for the NCEP global model. *Tellus* 60A, 113-
1124 130.

1125 Tiedtke M., 1989: A comprehensive mass flux scheme for cumulus parameterisation in large-
1126 scale models. *Mon. Wea. Rev.* 117, 1779-1799.

1127 Vukicevic, T., T. Greenwald, M. Zupanski, D. Zupanski, T. Vonder Haar, and A. S. Jones, 2004:
1128 Mesoscale cloud state estimation from visible and infrared satellite radiances. *Mon. Wea. Rev.*,
1129 132, 3066–3077, doi:10.1175/MWR2837.1.

1130 Vukicevic, T., M. Sengupta, A. S. Jones, and T. Vonder Haar, 2006: Cloud- resolving satellite
1131 data assimilation: Information content of IR window observations and uncertainties in estimation.
1132 *J. Atmos. Sci.*, 63, 901–919, doi:10.1175/JAS3639.1.

1133 Wang, P., J. Li, B. Lu, T. J. Schmit, J. Lu, Y.-K. Lee, J. Li, and Z. Liu, 2018: Im-
1134 pact of moisture information from Advanced Himawari Imager measurements on heavy pre-
1135 cipitation forecasts in a regional NWP model. *J. Geophys Res. Atmos.*, 123, 6022–6038.
1136 <https://doi.org/10.1029/2017JD028012>.

1137 Wu, T.-C., M. Zupanski, L. D. Grasso, C. D. Kummerow, and S.-A. Boukabara, 2019: All-sky
1138 radiance assimilation of ATMS in HWRF: A demonstration study. *Mon. Wea. Rev.*, 147, 85-106.

1139 Yang, P., L. Bi, B. A. Baum, K.-N. Liou, G. Kattawar, M. Mishchenko, and B. Cole, 2013:
1140 Spectrally consistent scattering, absorption, and polarization properties of atmospheric ice crystals
1141 at wavelengths from 0.2 μm to 100 μm . *J. Atmos. Sci.*, 70, 330-347.

1142 Yang C., Z. Liu, J. Bresch, S. R. Rizvi, X. Y. Huang, and J. Min, 2016: AMSR2 all-sky radiance
1143 assimilation and its impact on the analysis and forecast of hurricane Sandy with a limited-area data
1144 assimilation system. *Tellus A*, 68, 30917, <http://dx.doi.org/10.3402/tellusa.v68.30917>.

1145 Yi, B., P. Yang, Q. Liu, P. van Delst, S.-A. Boukabara, and F. Weng, 2016: Improvements on the
1146 ice cloud modeling capabilities of the Community Radiative Transfer Model. *J. Geophys. Res.*
1147 *Atmos.*, 121, 13,577–13,590, doi:10.1002/2016JD025207.

1148 Zangl G., D. Reinert, P. Ripodas, and M. Baldauf, 2015: The ICON (ICOsahedral Non-
1149 hydrostatic) modelling framework of DWD and MPI-M: Description of the non-hydrostatic dy-
1150 namical core. *Q. J. R. Meteorol. Soc.*, 141, 563-579, doi:10.1002/qj.2378.

1151 Zhang F., C. Snyder, and J. Sun, 2004: Impacts of initial estimate and observation availability
1152 on convective-scale data assimilation with an ensemble Kalman filter. *Mon. Wea. Rev.*, 132,
1153 1238-1253.

1154 Zhang, F., M. Minamide, and E. Clothiaux, 2016: Potential impacts of assimilating all-sky in-
1155 frared satellite radiances from GOES-R on convection-permitting analysis and prediction of trop-
1156 ical cyclones. *Geophys. Res. Lett.*, 43, 2954–2963, <https://doi.org/10.1002/2016GL068468>.

1157 Zhang, Y. J., F. Q. Zhang, and D. J. Stensrud, 2018: Assimilating All-Sky Infrared Radiances
1158 from GOES-16 ABI Using an Ensemble Kalman Filter for Convection-Allowing Severe Thunder-
1159 storms Prediction. *Mon. Wea. Rev.*, 146, 3363-3381.

1160 Zhang, M., F. Zhang, X.-Y. Huang, and X. Zhang, 2011: Intercomparison of an ensem-
1161 ble Kalman filter with three- and four-dimensional variational data assimilation methods in
1162 a limited-area model over the month of June 2003. *Mon. Wea. Rev.*, 139, 566–572,
1163 <https://doi.org/10.1175/2010MWR3610.1>.

1164 Zhang, S., and L. Guan, 2017: Preliminary study on direct assimilation of cloud-affected satellite
1165 brightness temperatures. *Adv. Atmos. Sci.*, 34, 199-208.

1166 Zhu Y., J. Derber, A. Collard, D. Dee, R. Treadon, G. Gayno, and J. A. Jung, 2014: En-
1167 hanced radiance bias correction in the National Centers for Environmental Prediction’s Grid-
1168 point Statistical Interpolation data assimilation system. *Q. J. R. Meteorol. Soc.*, 140, 1479-1492,
1169 doi:10.1002/qj.2233.

1170 Zhu, Y., and Coauthors, 2016: All-sky microwave radiance assimilation in NCEP’s GSI analysis
1171 system. *Mon. Wea. Rev.*, 144, 4709-4735.

1172 Zupanski, D., M. Zupanski, L. D. Grasso, R. Brummer, I. Jankov, D. Lindsey, M.
1173 Sengupta, and M. Demaria, 2011: Assimilating synthetic GOES-R radiances in cloudy
1174 conditions using an ensemble-based method. *Int. J. Remote Sens.*, 32, 9637–9659,
1175 doi:10.1080/01431161.2011.572094.

1176 **6. Figure Captions**

1177 Fig. 1. Observed SEVIRI 6.2 μm brightness temperatures (K) valid at (a) 06 UTC on 28 May,
1178 (b) 18 UTC on 28 May, (c) 06 UTC on 29 May, (d) 18 UTC on 29 May, (e) 06 UTC on 30 May,
1179 and (f) 18 UTC on 30 May 2014.

1180 Fig. 2. (a) Probability distribution of SEVIRI 6.2 μm observation-minus-background (O-B)
1181 brightness temperature departures (K) for the No-Assim experiment plotted as a function of the
1182 observed 6.2 μm brightness temperatures (K). (b-e) Probability distributions of SEVIRI 6.2 μm
1183 ensemble mean brightness temperature bias corrections (K) for the OBSCTH-0TH, OBSCTH-
1184 1ST, OBSCTH-2ND, and OBSCTH-3RD experiments plotted as a function of the observed 6.2
1185 μm brightness temperatures (K). Data were accumulated at hourly intervals during a 72-h period
1186 from 00 UTC on 28 May 2014 to 00 UTC on 31 May 2014. The horizontal purple lines shows
1187 the mean O-B departure (panel a) or the mean bias correction (panels b-e), whereas the black line
1188 segments depict the conditional O-B bias (panel a) or the mean bias correction (panels b-e) in each
1189 column.

1190 Fig. 3. Time series showing the evolution of the SEVIRI 6.2 μm brightness temperature (a)
1191 bias (K) and (b) root mean square error (RMSE; K) computed using the ensemble mean prior
1192 analysis at hourly intervals from 00 UTC on 28 May 2014 to 00 UTC on 31 May 2014. Results
1193 are shown for the No-BC (dashed black line), OBSCTH-3RD (red line), OBSCTH-2ND (blue

1194 line), OBSCTH-1ST (green line), OBSCTH-0TH (magenta line), and No-Assim (solid black line)
1195 experiments

1196 Fig. 4. (a) Vertical profiles of temperature root mean square error (RMSE; K) from the No-
1197 Assim (black) and No-BC experiments (dashed black), with percentage changes in RMSE for
1198 the OBSCTH-3RD (red), OBSCTH-2ND (blue), OBSCTH-1ST (green), and OBSCTH-0TH (ma-
1199 genta) experiments relative to the No-Assim and No-BC experiments shown in panels (b) and
1200 (c). (d-f) Same as (a-c) except for showing vertical profiles of relative humidity RMSE (%). (g-i)
1201 Same as (a-c) except for showing vertical profiles of zonal wind speed RMSE (m s-1). (j-l) Same
1202 as (a-c) except for showing vertical profiles of meridional wind speed RMSE (m s-1). The error
1203 profiles were computed using data from the prior analyses over a 3-day period from 00 UTC on
1204 28 May 2014 to 00 UTC on 31 May 2014.

1205 Fig. 5. Vertical profiles of (a) temperature bias (K), (b) relative humidity bias (%), (c) zonal wind
1206 speed bias (m s-1), and (d) meridional wind speed bias (m s-1) for the No-Assim (solid black),
1207 No-BC (dashed black), OBSCTH-3RD (red), OBSCTH-2ND (blue), OBSCTH-1ST (green), and
1208 OBSCTH-0TH (magenta) experiments. The error profiles were computed using data from the
1209 prior analyses over a 3-day period from 01 UTC on 28 May 2014 to 00 UTC on 31 May 2014.

1210 Fig. 6. Time series showing the evolution of the SEVIRI 6.2 μm brightness temperature (a) bias
1211 (K), (b) root mean square error (RMSE; K), (c) spread (K), and (d) consistency ratio computed
1212 using the ensemble mean prior analysis at hourly intervals from 00 UTC on 28 May 2014 to 00
1213 UTC on 31 May 2014. Results are shown for the No-BC (dashed black line), BC-OBSCTH (red
1214 line), BC-OBSBT (blue line), BC-IWC (green line), BC-SATZEN (magenta line), and No-Assim
1215 (solid black line) experiments.

1216 Fig. 7. Probability distribution of SEVIRI 6.2 μm ensemble mean brightness temperature cor-
1217 rections (K) from the (a) BC-OBSBT, (b) BC-OBSCTH, (c) BC-IWC, and (d) BC-SATZEN ex-

1218 periments plotted as a function of the observed $6.2 \mu\text{m}$ brightness temperatures. Data were accu-
1219 mulated at hourly intervals during a 72-h period from 01 UTC on 28 May 2014 to 00 UTC on 31
1220 May 2014. The horizontal black line segments represent the conditional bias in each column.

1221 Fig. 8. Probability distributions of SEVIRI $6.2 \mu\text{m}$ brightness temperature innovations (K)
1222 for the (a) No-Assim, (b) No-BC, (c) BC-OBSBT, (d) BC-OBSCTH, (e) BC-IWC, and (f) BC-
1223 SATZEN experiments plotted as a function of the observed $6.2 \mu\text{m}$ brightness temperatures (K).
1224 Data were accumulated at hourly intervals from 00 UTC on 28 May 2014 to 00 UTC on 31 May
1225 2014. The black line segments depict the mean innovation in each column.

1226 Fig. 9. (a) Vertical profiles of temperature root mean square error (RMSE; K) from the No-
1227 Assim (solid black) and No-BC experiments (dashed black), with percentage changes in RMSE
1228 for the BC-OBSBT (blue), BC-OBSCTH (red), BC-IWC (green), and BC-SATZEN (magenta)
1229 experiments relative to the No-Assim and No-BC experiments shown in panels (b) and (c). (d-f)
1230 Same as (a-c) except for showing vertical profiles of relative humidity RMSE (%). (g-i) Same as
1231 (a-c) except for showing vertical profiles of zonal wind speed RMSE (m s^{-1}). (j-l) Same as (a-c)
1232 except for showing vertical profiles of meridional wind speed RMSE (m s^{-1}). The error profiles
1233 were computed using data from the ensemble mean prior analyses at hourly over a 3-day period
1234 from 00 UTC on 28 May 2014 to 00 UTC on 31 May 2014.

1235 Fig. 10. Vertical profiles of (a) temperture bias (K), (b) relative humidity bias (%), (c) zonal
1236 wind speed bias (m s^{-1}), and (d) meridional wind speed bias (m s^{-1}) for the No-Assim (solid
1237 black), No-BC (dashed black), BC-OBSBT (blue), BC-OBSCTH (red), BC-IWC (green), and
1238 BC-SATZEN (magenta) experiments. The error profiles were computed using data from the prior
1239 analyses over a 3-day period from 01 UTC on 28 May 2014 to 00 UTC on 31 May 2014.

1240 Fig. 11. Probability distributions for the SEVIRI $6.2 \mu\text{m}$ brightness temperature (a) bias correc-
1241 tions and (b) innovations from the BC-SIMCTH experiment plotted as a function of the observed

1242 6.2 μm brightness temperatures (K). (c-d) Same as (a-b), except for the BC-SYMCTH experiment.
1243 (e-f) Same as (a-b), except for the BC-OBSCTH experiment. Data were accumulated at hourly
1244 intervals from 00 UTC on 28 May 2014 to 00 UTC on 31 May 2014. The black line segments
1245 depict the mean bias correction or innovation in each column.

7. Figures

LIST OF TABLES

1248	Table 1.	Percentage changes in root mean square error (RMSE) and bias for the zonal and meridional wind speed, temperature, and relative humidity for the OBSCTH-0TH, OBSCTH-1ST, OBSCTH-2ND, and OBSCTH-3RD experiments relative to the No-BC experiment. The statistics were computed using all of the radiosonde observations and output from the prior ensemble mean analyses during the 72-h assimilation period.	58
1249			
1250			
1251			
1252			
1253			
1254	Table 2.	Percentage changes in root mean square error (RMSE) and bias for the zonal and meridional wind speed, temperature, and relative humidity for the BC-OBSBT, BC-OBSCTH, BC-IWC, and BC-SATZEN experiments relative to the No-Assim experiment. The statistics were computed using all of the radiosonde observations and output from the prior ensemble mean analyses during the 72-hr assimilation period.	59
1255			
1256			
1257			
1258			
1259			
1260	Table 3.	Percentage changes in root mean square error (RMSE) and bias for the zonal and meridional wind speed, temperature, and relative humidity for the BC-OBSBT, BC-OBSCTH, BC-IWC, and BC-SATZEN experiments relative to the No-BC experiment. The statistics were computed using all of the radiosonde observations and output from the prior ensemble mean analyses during the 72-hr assimilation period.	60
1261			
1262			
1263			
1264			
1265			
1266	Table 4.	Percentage changes in root mean square error (RMSE) and bias for the zonal and meridional wind speed, temperature, and relative humidity for the BC-OBSBT, BC-SYMBT, and BC-SIMBT experiments relative to the No-BC experiment. The statistics were computed using all of the radiosonde observations and output from the prior ensemble mean analyses during the 72-h assimilation period.	61
1267			
1268			
1269			
1270			
1271			
1272	Table 5.	Percentage changes in root mean square error (RMSE) and bias for the zonal and meridional wind speed, temperature, and relative humidity for the BC-OBSCTH, BC-SYMCTH, and BC-SIMCTH experiments relative to the No-BC experiment. The statistics were computed using all of the radiosonde observations and output from the prior ensemble mean analyses during the 72-h assimilation period.	62
1273			
1274			
1275			
1276			
1277			

1278 TABLE 1. Percentage changes in root mean square error (RMSE) and bias for the zonal and meridional
 1279 wind speed, temperature, and relative humidity for the OBSCTH-0TH, OBSCTH-1ST, OBSCTH-2ND, and
 1280 OBSCTH-3RD experiments relative to the No-BC experiment. The statistics were computed using all of the
 1281 radiosonde observations and output from the prior ensemble mean analyses during the 72-h assimilation period.

	U	V	T		RH	
EXP	RMSE	RMSE	RMSE	BIAS	RMSE	BIAS
OBSCTH-0TH - No-BC	-0.2%	-0.2%	-0.1%	-4.7%	-0.6%	-36.2%
OBSCTH-1ST - No-BC	-0.7%	-0.1%	-0.3%	-3.1%	-0.9%	-29.1%
OBSCTH-2ND - No-BC	-0.9%	-0.5%	-0.3%	-5.0%	-1.5%	-25.6%
OBSCTH-3RD - No-BC	-1.0%	-0.8%	-0.2%	-1.3%	-1.8%	-30.2%

1282 TABLE 2. Percentage changes in root mean square error (RMSE) and bias for the zonal and meridional
 1283 wind speed, temperature, and relative humidity for the BC-OBSBT, BC-OBSCTH, BC-IWC, and BC-SATZEN
 1284 experiments relative to the No-Assim experiment. The statistics were computed using all of the radiosonde
 1285 observations and output from the prior ensemble mean analyses during the 72-hr assimilation period.

	U	V	T		RH	
EXP	RMSE	RMSE	RMSE	BIAS	RMSE	BIAS
No-BC - No-Assim	0.9%	0.6%	1.0%	-1.7%	0.8%	30.1%
BC-OBSBT - No-Assim	0.0%	-0.8%	0.8%	-4.7%	-0.4%	9.8%
BC-OBSCTH - No-Assim	-0.1%	-0.2%	0.8%	-3.0%	-1.0%	-9.2%
BC-IWC - No-Assim	0.7%	0.6%	0.9%	-4.8%	-0.1%	-28.8%
BC-SATZEN - No-Assim	0.8%	0.5%	1.0%	-6.1%	-0.6%	-19.6%

1286 TABLE 3. Percentage changes in root mean square error (RMSE) and bias for the zonal and meridional wind
 1287 speed, temperature, and relative humidity for the BC-OBSBT, BC-OBSCTH, BC-IWC, and BC-SATZEN exper-
 1288 iments relative to the No-BC experiment. The statistics were computed using all of the radiosonde observations
 1289 and output from the prior ensemble mean analyses during the 72-hr assimilation period.

	U	V	T		RH	
EXP	RMSE	RMSE	RMSE	BIAS	RMSE	BIAS
BC-OBSBT - No-BC	-0.9%	-1.4%	-0.2%	-3.1%	-1.2%	-15.6%
BC-OBSCTH - No-BC	-1.0%	-0.8%	-0.2%	-1.3%	-1.8%	-30.2%
BC-IWC - No-BC	-0.2%	0.0%	-0.1%	-3.2%	-0.9%	-45.2%
BC-SATZEN - No-BC	-0.1%	-0.1%	0.1%	-4.5%	-1.4%	-38.2%

1290 TABLE 4. Percentage changes in root mean square error (RMSE) and bias for the zonal and meridional
 1291 wind speed, temperature, and relative humidity for the BC-OBSBT, BC-SYMBT, and BC-SIMBT experiments
 1292 relative to the No-BC experiment. The statistics were computed using all of the radiosonde observations and
 1293 output from the prior ensemble mean analyses during the 72-h assimilation period.

	U	V	T		RH	
EXP	RMSE	RMSE	RMSE	BIAS	RMSE	BIAS
BC-OBSBT - No-BC	-0.9%	-1.4%	-0.2%	-3.1%	-1.2%	-15.6%
BC-SYMBT - No-BC	-0.1%	0.0%	-0.1%	-2.0%	-1.0%	-29.6%
BC-SIMBT - No-BC	1.0%	1.3%	0.6%	-1.1%	-0.8%	-55.8%

1294 TABLE 5. Percentage changes in root mean square error (RMSE) and bias for the zonal and meridional wind
 1295 speed, temperature, and relative humidity for the BC-OBSCTH, BC-SYMCTH, and BC-SIMCTH experiments
 1296 relative to the No-BC experiment. The statistics were computed using all of the radiosonde observations and
 1297 output from the prior ensemble mean analyses during the 72-h assimilation period.

	U	V	T		RH	
EXP	RMSE	RMSE	RMSE	BIAS	RMSE	BIAS
BC-OBSCTH - No-BC	-1.0%	-0.8%	-0.2%	-1.3%	-1.8%	-30.2%
BC-SYMCTH - No-BC	-0.4%	-0.5%	0.0%	-3.1%	-1.2%	-27.1%
BC-SIMCTH - No-BC	-0.2%	0.5%	0.0%	-1.2%	-1.5%	-43.2%

1298 **LIST OF FIGURES**

1299 **Fig. 1.** 64

1300 **Fig. 2.** 65

1301 **Fig. 3.** 66

1302 **Fig. 4.** 67

1303 **Fig. 5.** 68

1304 **Fig. 6.** 69

1305 **Fig. 7.** 70

1306 **Fig. 8.** 71

1307 **Fig. 9.** 72

1308 **Fig. 10.** 73

1309 **Fig. 11.** 74

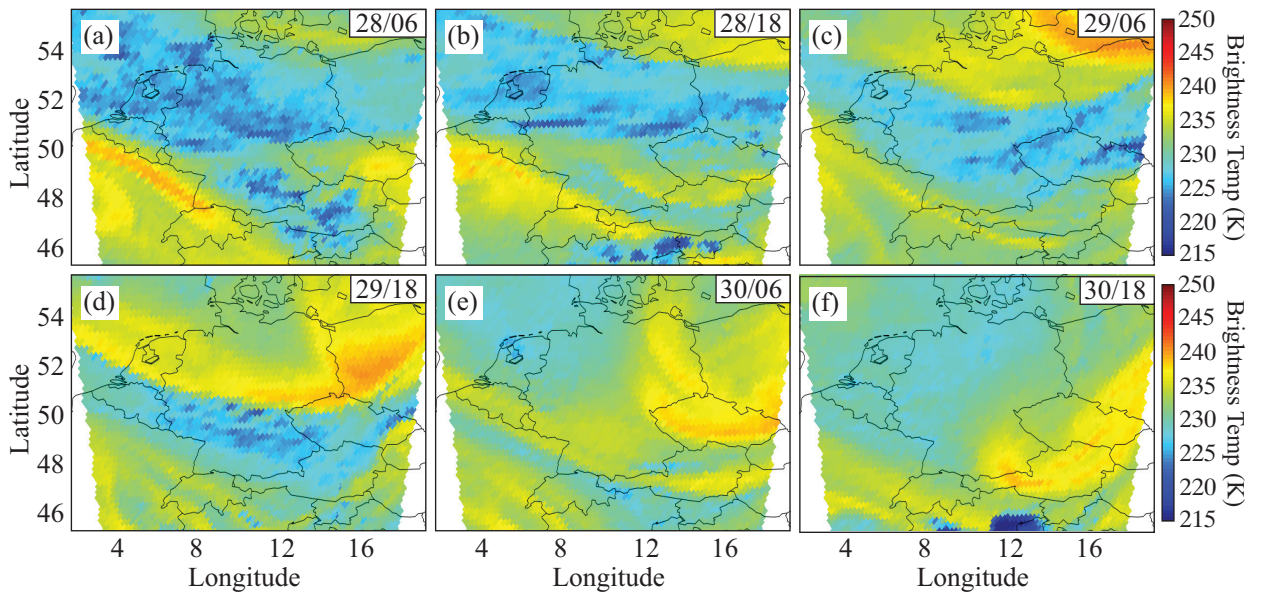


Fig. 1. Observed SEVIRI 6.2 μm brightness temperatures (K) valid at (a) 06 UTC on 28 May, (b) 18 UTC on 28 May, (c) 06 UTC on 29 May, (d) 18 UTC on 29 May, (e) 06 UTC on 30 May, and (f) 18 UTC on 30 May 2014.

FIG. 1.

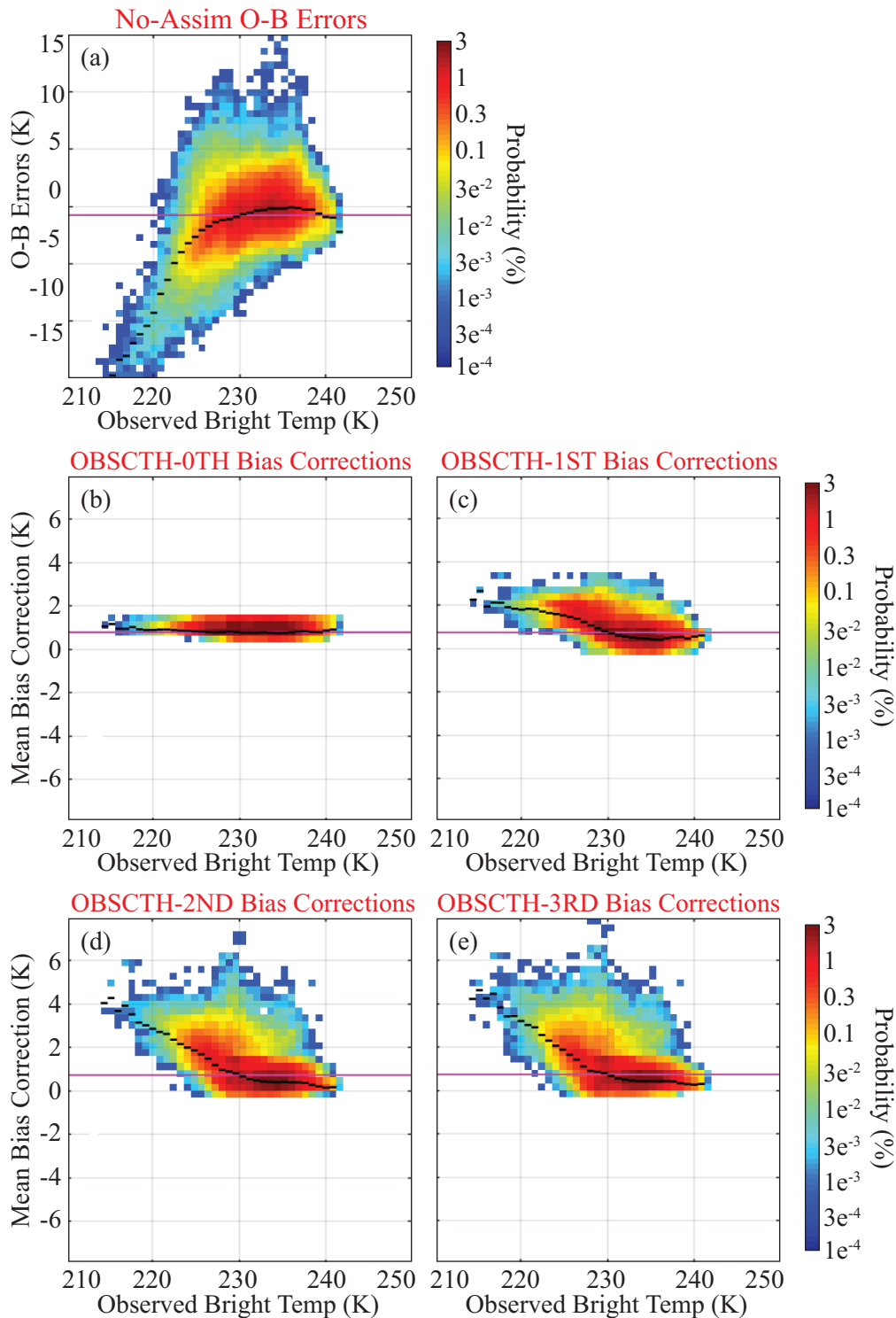


Fig. 2. (a) Probability distribution of SEVIRI 6.2 μm observation-minus-background (O-B) brightness temperature departures (K) for the No-Assim experiment plotted as a function of the observed 6.2 μm brightness temperatures (K). (b-e) Probability distributions of SEVIRI 6.2 μm ensemble mean brightness temperature bias corrections (K) for the OBSCTH-0TH, OBSCTH-1ST, OBSCTH-2ND, and OBSCTH-3RD experiments plotted as a function of the observed 6.2 μm brightness temperatures (K). Data were accumulated at hourly intervals during a 72-h period from 00 UTC on 28 May 2014 to 00 UTC on 31 May 2014. The horizontal purple lines shows the mean O-B departure (panel a) or the mean bias correction (panels b-e), whereas the black line segments depict the conditional O-B bias (panel a) or the mean bias correction (panels b-e) in each column.

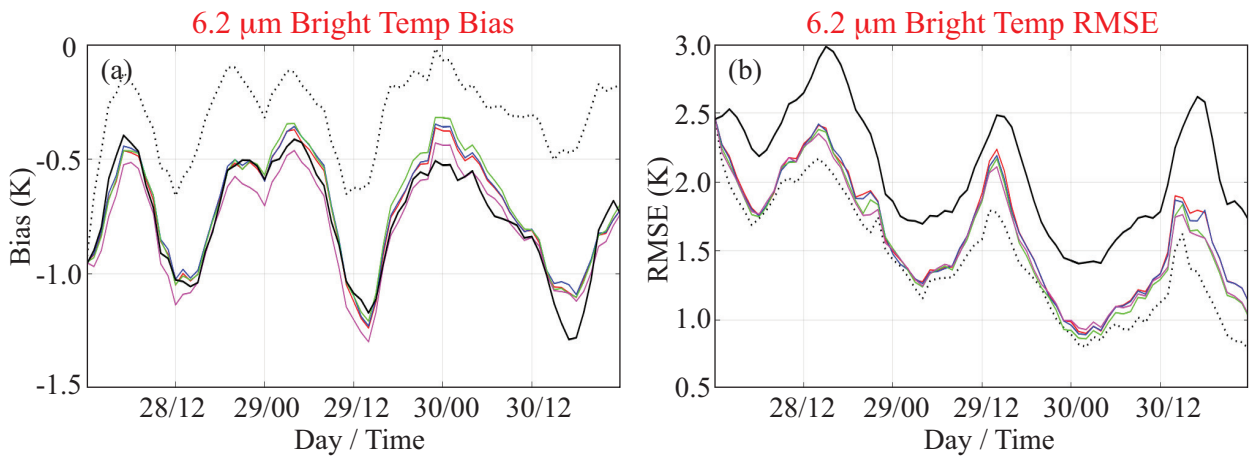


Fig. 3. Time series showing the evolution of the SEVIRI 6.2 μm brightness temperature (a) bias (K) and (b) root mean square error (RMSE; K) computed using the ensemble mean prior analysis at hourly intervals from 00 UTC on 28 May 2014 to 00 UTC on 31 May 2014. Results are shown for the No-BC (dashed black line), OBSCTH-3RD (red line), OBSCTH-2ND (blue line), OBSCTH-1ST (green line), OBSCTH-0TH (magenta line), and No-Assim (solid black line) experiments.

FIG. 3.

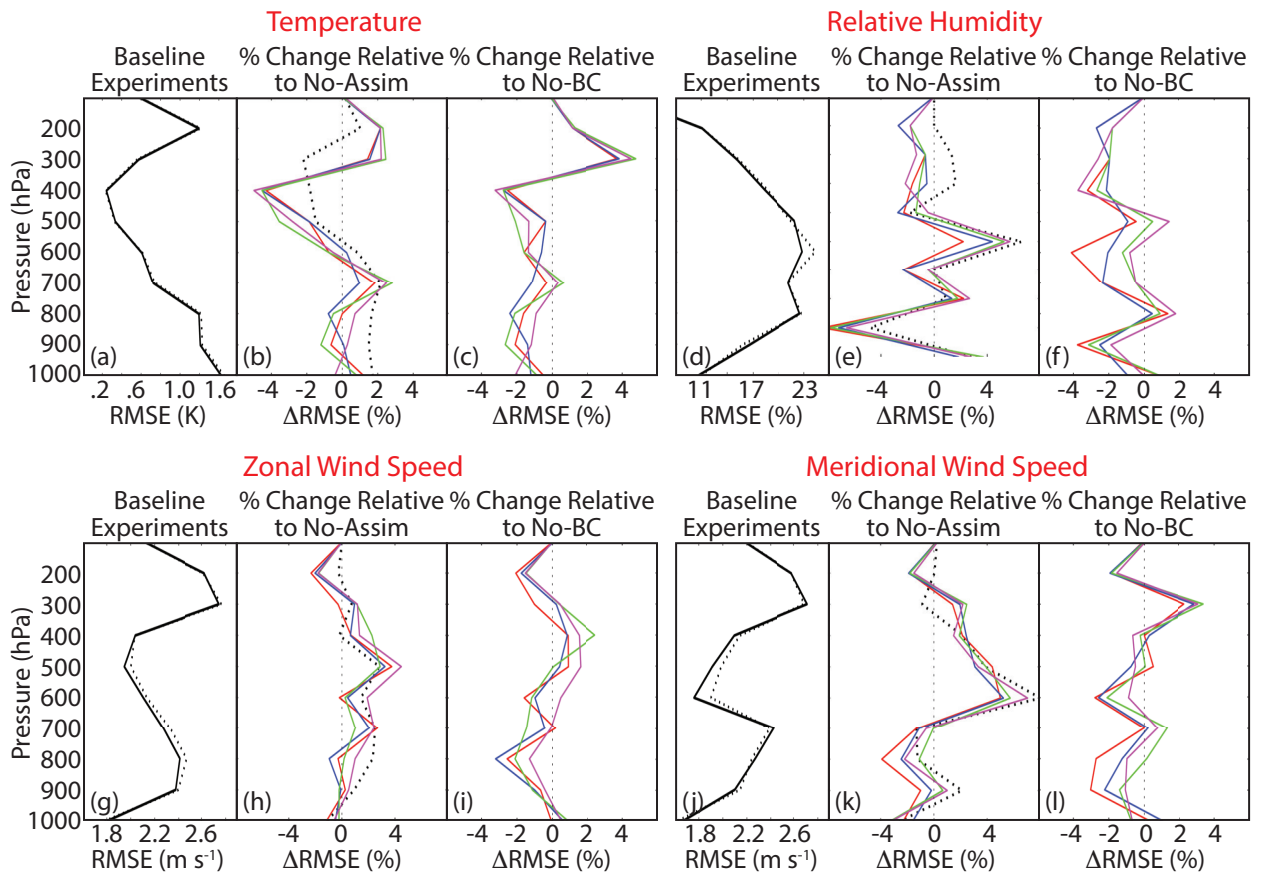


Fig. 4. (a) Vertical profiles of temperature root mean square error (RMSE; K) from the No-Assim (black) and No-BC experiments (dashed black), with percentage changes in RMSE for the OBSCTH-3RD (red), OBSCTH-2ND (blue), OBSCTH-1ST (green), and OBSCTH-0TH (magenta) experiments relative to the No-Assim and No-BC experiments shown in panels (b) and (c). (d-f) Same as (a-c) except for showing vertical profiles of relative humidity RMSE (%). (g-i) Same as (a-c) except for showing vertical profiles of zonal wind speed RMSE (m s^{-1}). (j-l) Same as (a-c) except for showing vertical profiles of meridional wind speed RMSE (m s^{-1}). The error profiles were computed using data from the prior analyses over a 3-day period from 00 UTC on 28 May 2014 to 00 UTC on 31 May 2014.

FIG. 4.

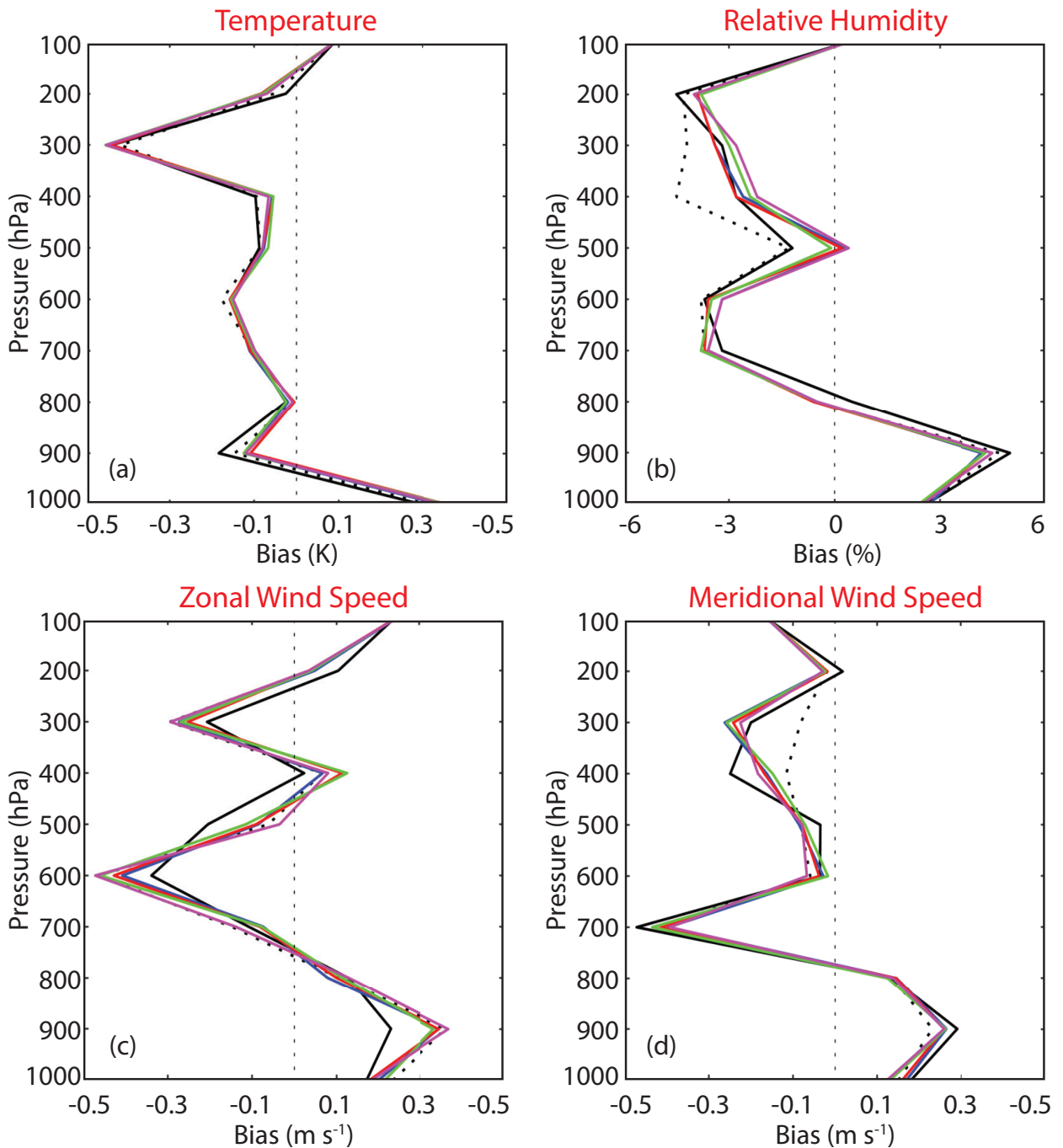


Fig. 5. Vertical profiles of (a) temperature bias (K), (b) relative humidity bias (%), (c) zonal wind speed bias (m s^{-1}), and (d) meridional wind speed bias (m s^{-1}) for the No-Assim (solid black), No-BC (dashed black), OBSCTH-3RD (red), OBSCTH-2ND (blue), OBSCTH-1ST (green), and OBSCTH-0TH (magenta) experiments. The error profiles were computed using data from the prior analyses over a 3-day period from 01 UTC on 28 May 2014 to 00 UTC on 31 May 2014.

FIG. 5.

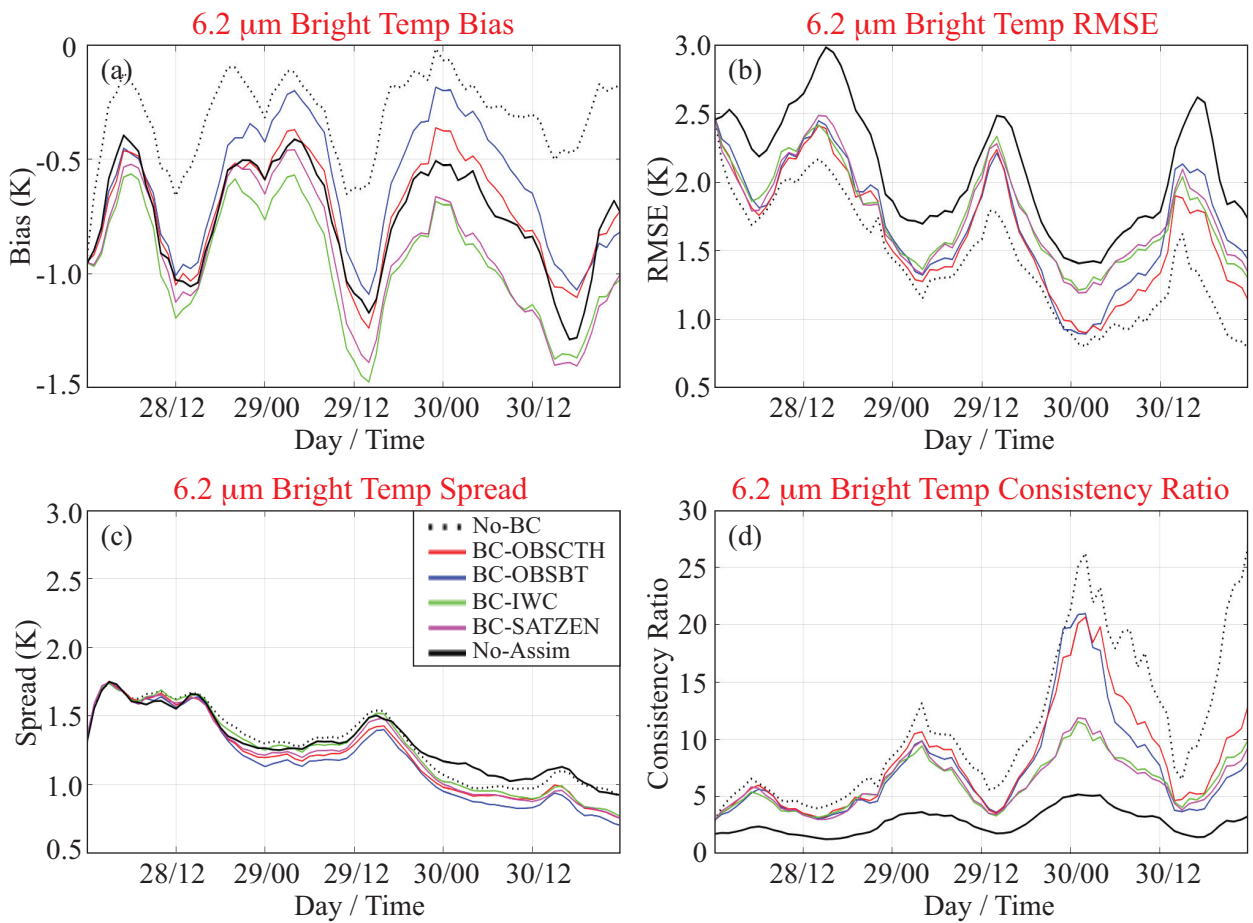


Fig. 6. Time series showing the evolution of the SEVIRI 6.2 μm brightness temperature (a) bias (K), (b) root mean square error (RMSE; K), (c) spread (K), and (d) consistency ratio computed using the ensemble mean prior analysis at hourly intervals from 00 UTC on 28 May 2014 to 00 UTC on 31 May 2014. Results are shown for the No-BC (dashed black line), BC-OBSCTH (red line), BC-OBSBT (blue line), BC-IWC (green line), BC-SATZEN (magenta line), and No-Assim (solid black line) experiments.

FIG. 6.

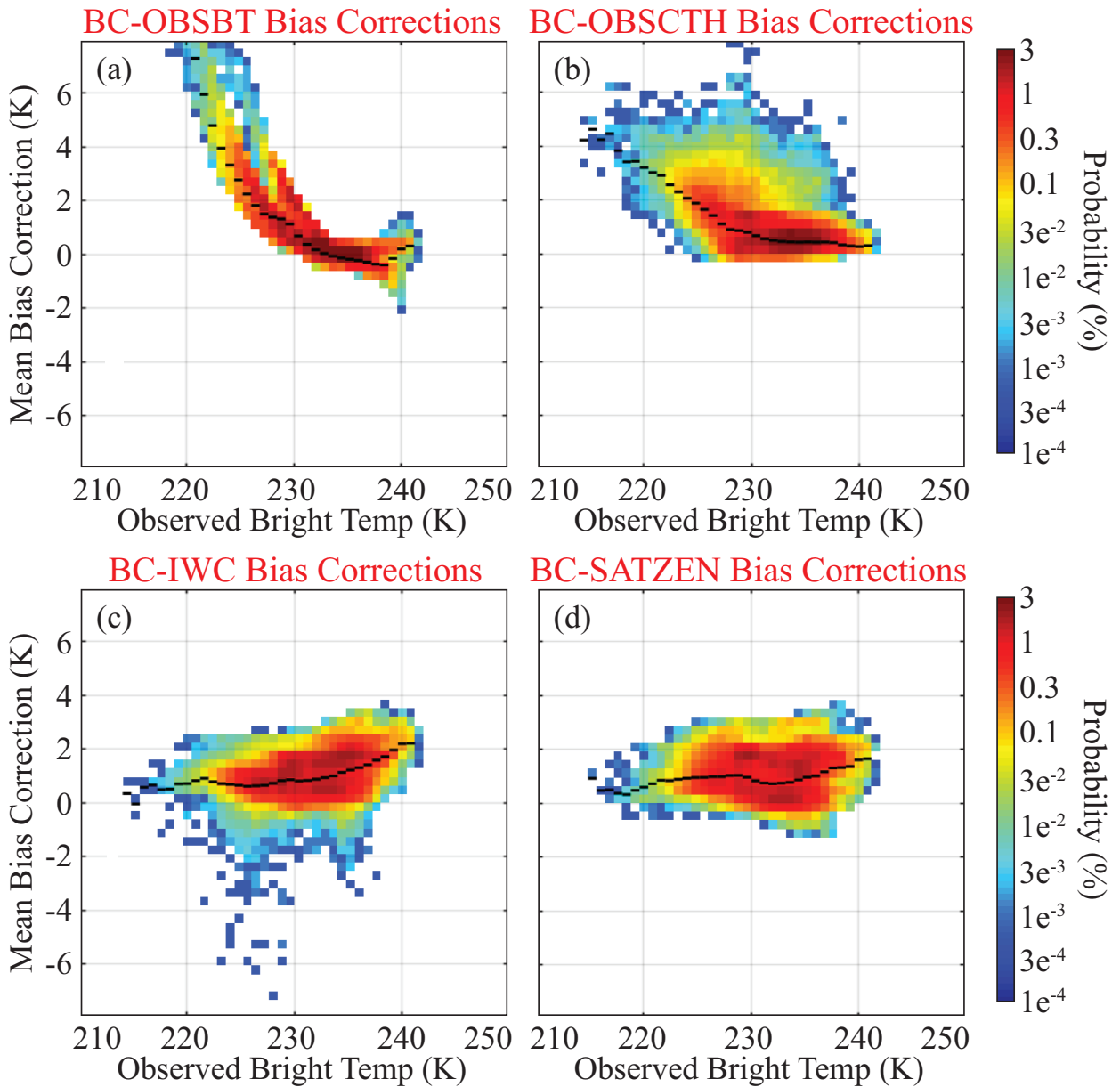


Fig. 7. Probability distribution of SEVIRI 6.2 μm ensemble mean brightness temperature corrections (K) from the (a) BC-OBSBT, (b) BC-OBSCTH, (c) BC-IWC, and (d) BC-SATZEN experiments plotted as a function of the observed 6.2 μm brightness temperatures. Data were accumulated at hourly intervals during a 72-h period from 01 UTC on 28 May 2014 to 00 UTC on 31 May 2014. The horizontal black line segments represent the conditional bias in each column.

FIG. 7.

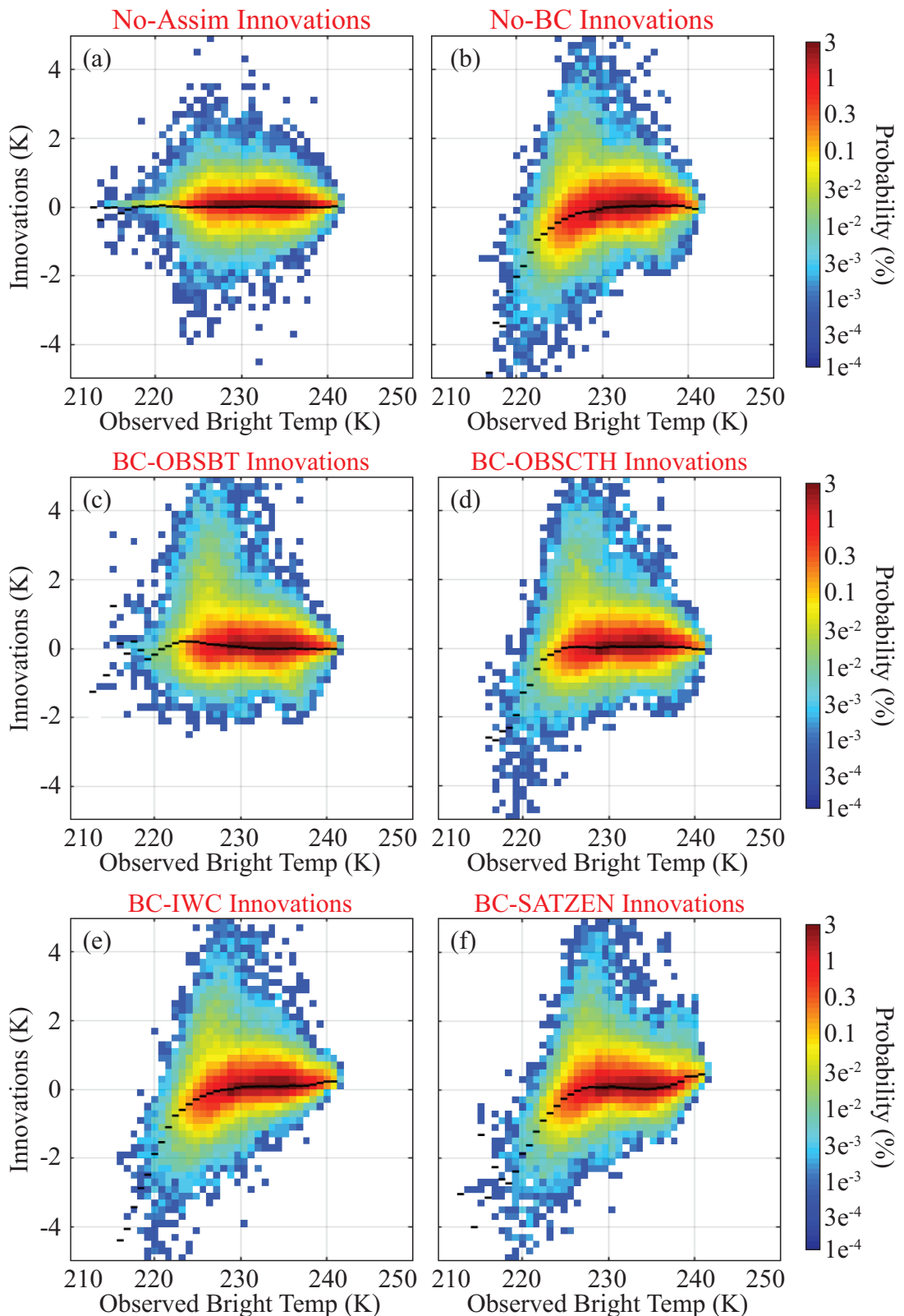


Fig. 8. Probability distributions of SEVIRI 6.2 μm brightness temperature innovations (K) for the (a) No-Assim, (b) No-BC, (c) BC-OBSBT, (d) BC-OBSCTH, (e) BC-IWC, and (f) BC-SATZEN experiments plotted as a function of the observed 6.2 μm brightness temperatures (K). Data were accumulated at hourly intervals from 00 UTC on 28 May 2014 to 00 UTC on 31 May 2014. The black line segments depict the mean innovation in each column.

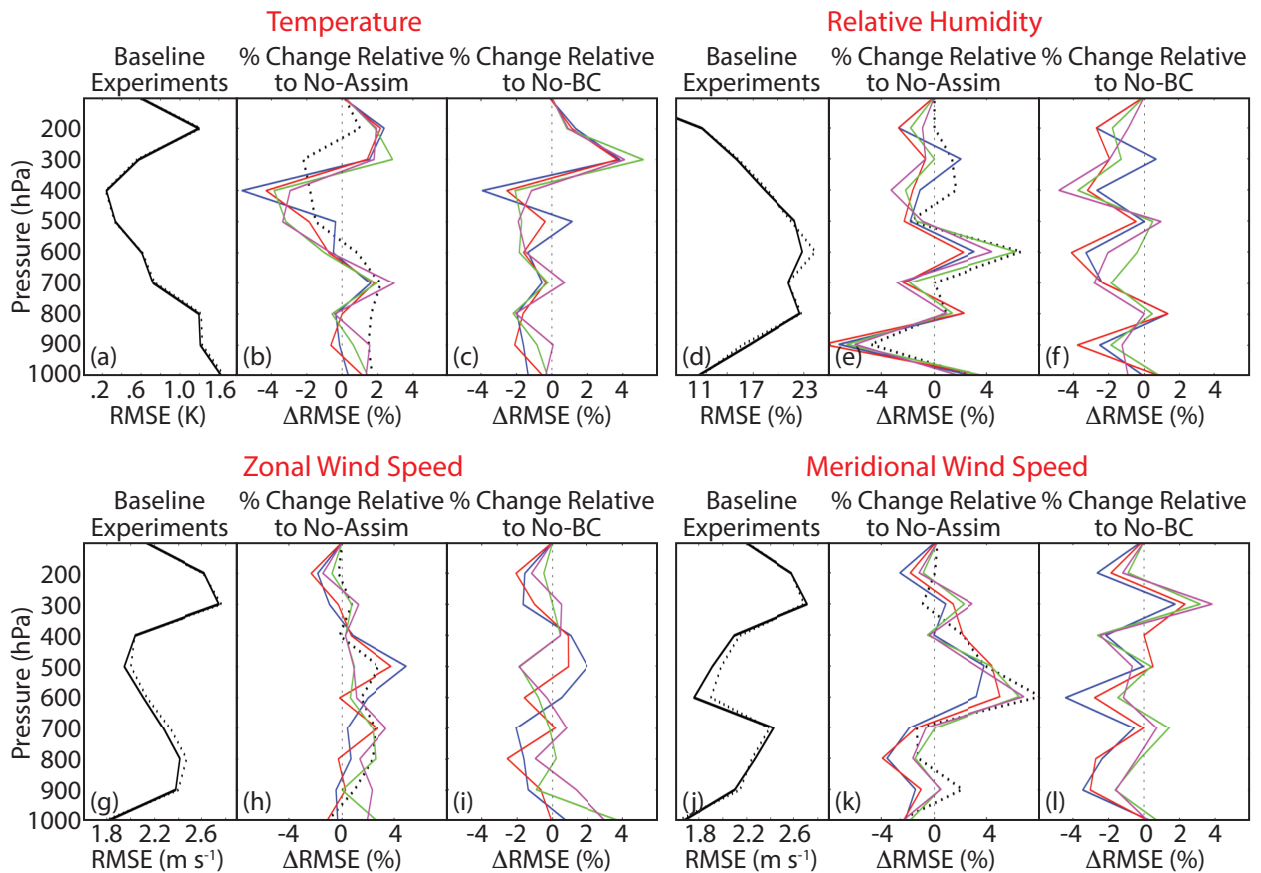


Fig. 9. (a) Vertical profiles of temperature root mean square error (RMSE; K) from the No-Assim (solid black) and No-BC experiments (dashed black), with percentage changes in RMSE for the BC-OBSBT (blue), BC-OBSCTH (red), BC-IWC (green), and BC-SATZEN (magenta) experiments relative to the No-Assim and No-BC experiments shown in panels (b) and (c). (d-f) Same as (a-c) except for showing vertical profiles of relative humidity RMSE (%). (g-i) Same as (a-c) except for showing vertical profiles of zonal wind speed RMSE (m s^{-1}). (j-l) Same as (a-c) except for showing vertical profiles of meridional wind speed RMSE (m s^{-1}). The error profiles were computed using data from the ensemble mean prior analyses at hourly over a 3-day period from 00 UTC on 28 May 2014 to 00 UTC on 31 May 2014.

FIG. 9.

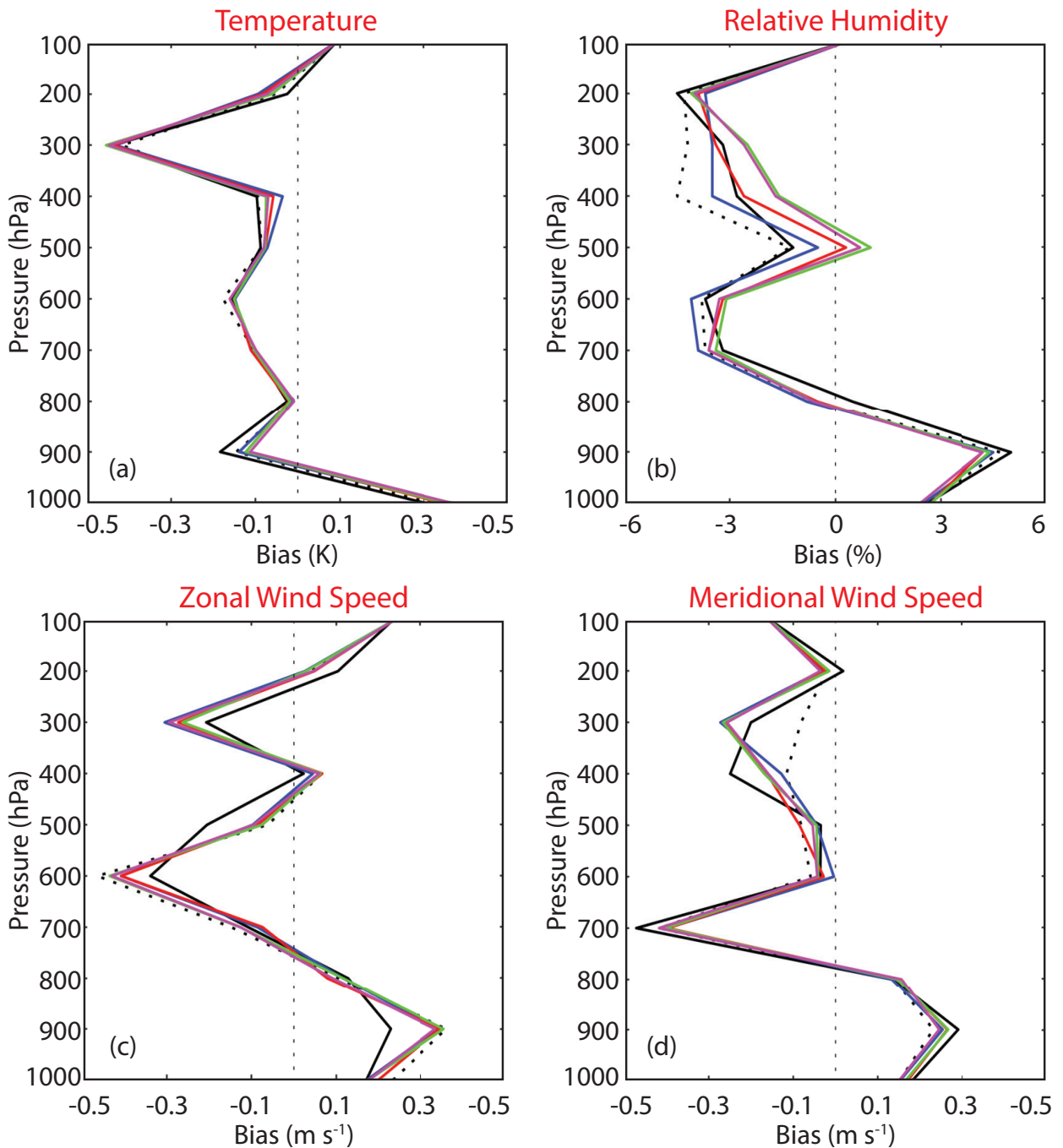


Fig. 10. Vertical profiles of (a) temperature bias (K), (b) relative humidity bias (%), (c) zonal wind speed bias (m s^{-1}), and (d) meridional wind speed bias (m s^{-1}) for the No-Assim (solid black), No-BC (dashed black), BC-OBSBT (blue), BC-OBSCTH (red), BC-IWC (green), and BC-SATZEN (magenta) experiments. The error profiles were computed using data from the prior analyses over a 3-day period from 01 UTC on 28 May 2014 to 00 UTC on 31 May 2014.

FIG. 10.

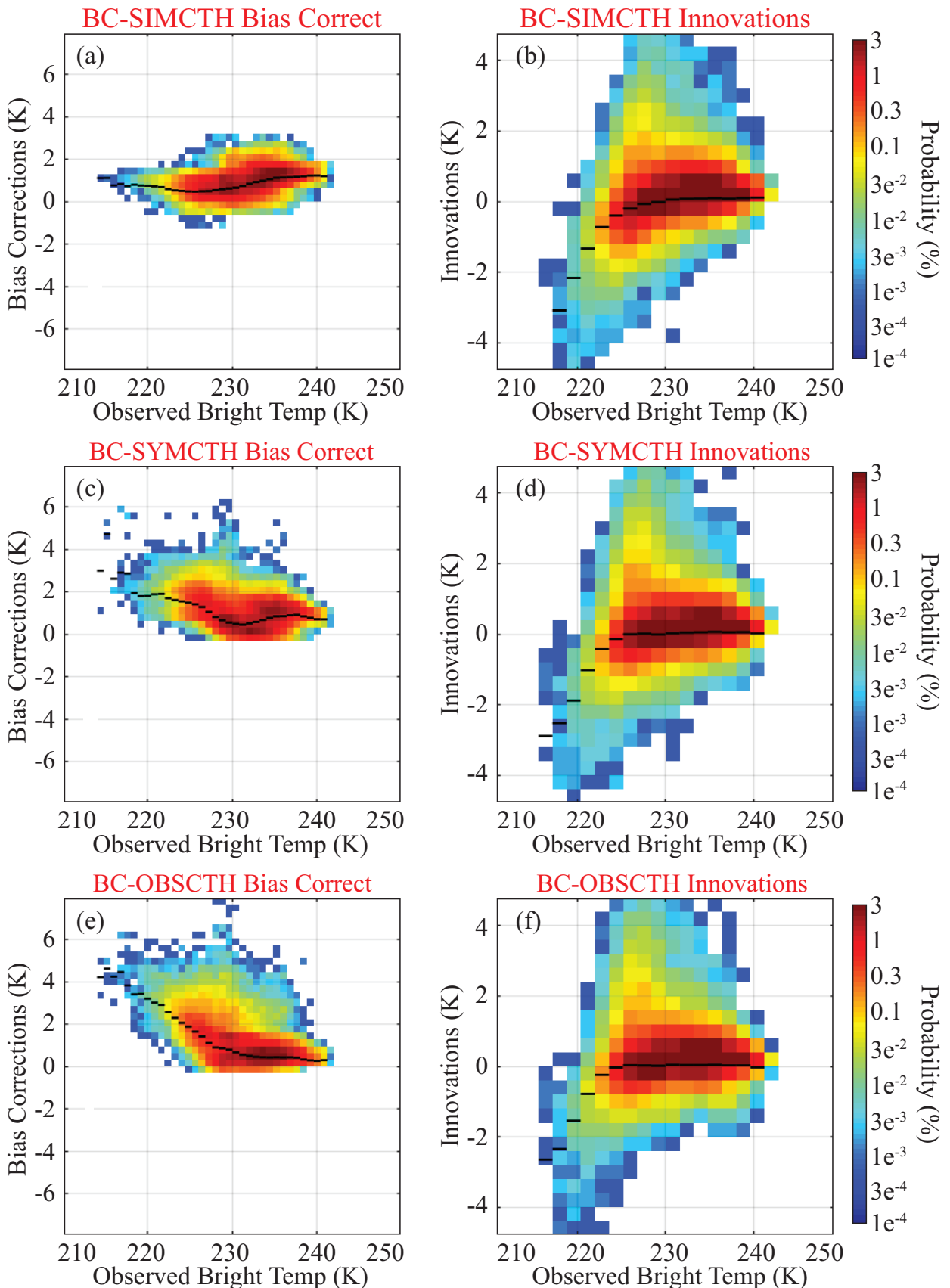


Fig. 11. Probability distributions for the SEVIRI 6.2 μm brightness temperature (a) bias corrections and (b) innovations from the BC-SIMCTH experiment plotted as a function of the observed 6.2 μm brightness temperatures (K). (c-d) Same as (a-b), except for the